TRIBHUVAN UNIVERSITY
INSTITUTE OF ENGINEERING
PULCHOWK CAMPUS

THESIS NO:M-95-MSMDE-2023-2025

Damage Detection in Composite Beams Using Modal Curvature Based Techniques

by
Aayush Bhatta

A THESIS
SUBMITTED TO THE DEPARTMENT OF MECHANICAL AND AEROSPACE ENGINEERING IN PARTIAL FULFILMENT OF THE REQUIREMENTS FOR THE DEGREE OF
MASTERS OF SCIENCE IN MECHANICAL SYSTEMS DESIGN AND ENGINEERING

DEPARTMENT OF MECHANICAL AND AEROSPACE ENGINEERING
LALITPUR, NEPAL

APRIL, 2025

COPYRIGHT

TRIBHUVAN UNIVERSITY
INSTITUTE OF ENGINEERING
PULCHOWK CAMPUS
DEPARTMENT OF MECHANICAL AND AEROSPACE ENGINEERING

The undersigned certify that they have read and recommended to the Department of Mechanical and Aerospace Engineering for acceptance, a dissertation entitled "**Damage Detection in Fiber-Reinforced Polymer Composite Plates Under Different Thermal Load**", submitted by **Aayush Bhatta** in partial fulfillment of the requirements for the award of the degree of **Masters of Science in Mechanical Systems Design and Engineering**.

Asst. Prof. Sudip Bhattrai, Ph.D.
Supervisor,
Department of Mechanical and Aerospace Engineering

Er. Akin Chhetri
External Examiner,
Mechanical Engineer

Tribhuvan University
Institute of Engineering
Department of Mechanical and Aerospace Engineering
Pulchowk Campus

Committee Chairperson,
Asst. Prof. Dr. Sudip Bhattrai,
Head of Department,
Department of Mechanical and Aerospace Engineering

April 8, 2025

ABSTRACT

Delamination is a primary failure mode in laminated composite structures, leading to decreased stiffness and strength while also impacting their vibration behaviour. The detection of such occurrences is thus, considered necessary. This paper deals with detection of macro-level damage in E-Glass fibre/epoxy resin laminated composite beam using vibration-based detection method. In particular, this paper deals with the modal curvature based techniques for damage detection in composite beam. Firstly, the effect of delamination in dynamic characteristics of the beam is studied using FEM and verified through experimental measure. Then the experimental procedure is used to detect delamination and other forms of damages in the composite beam. Different modal curvature based techniques are discussed and finally compared to detect other form of damages such as hole and impact damage. It is found that of the techniques used, although external damage was detected with sufficient accuracy, the techniques detected internal delamination with poor accuracy.

Keywords: Modal curvature, Laminated composite, Damage detection, Vibration based damage detection

ACKNOWLEDGEMENT

I would like to express my deepest gratitude to Asst. Prof. Dr. Sudip Bhattrai for his expert supervision and unwavering support throughout my thesis work. My sincere thanks also go to Prof. Dr. Mahesh Chandra Luintel, Asst. Prof. Kamal Darlami, Asst. Prof. Bimal Rimal, and Er. Salim Maharjan for their invaluable guidance, motivation, and encouragement, which were instrumental in carrying out this research.

I am also grateful to the Department of Mechanical and Aerospace Engineering (DMAE) for providing the workspace, high-precision equipment, and resources necessary to conduct my experiments. I am especially thankful to Er.Chandrika Nand Adhikari and Er. Abhishek Bhandari for their assistance and support during the experimental phase, and to Er.Ghanshyam Aryal for his support throughout the documentation process.

Finally, I am deeply grateful to my family for their constant support. This achievement would not have been possible without them.

TABLE OF CONTENTS

LIST OF FIGURES

LIST OF TABLES

LIST OF ABBREVIATIONS

FGRP	Fibreglass Reinforced Polymer
PMC	Polymer Matrix Composites
EMA	Experimental Modal Analysis
OMA	Operational Modal Analysis
FRF	Frequency Response Function
DAQ	Data Acquisition System
BVID	Barely Visible Impact Damage
LLT	Laser Line Triangulation
TPR	True Positive
FPR	False Positive
ROC	Reciever Operating CHaracteristic
UV	Ultravoilet
ISO	International Organization for Standardization
VBDD	Vibration Based Damage Detection
ML	Machine Learning
DIC	Digital Image Correlation
DI	Damage Index
VBM	Vibration Based Methods
NDT	Non-destructive Technique
FRC	Fiber-reinforced Composite

LIST OF SYMBOLS

ω_n	natural frequency
ξ	Damping ratio
ϕ	Mode Shape
κ	Curvature
l_e	Length of an element
E_j	Element of a beam
E_j^*	Delaminated element of a beam
L_d	Length of the delaminated element
U_j	Strain energy of an element
D	Sectional bending stiffness
E	Young's modulus
$W(t)$	Modal amplitude
γ	Parameter related to structure's geometry
γ^*	Parameter related to structure's geometry for damaged element
$\bar{D}$	Damage index
Γ	Total strain energy
$\beta_{C,j}$	Cornwell index
$\beta_{St,j}$	Stubbs index
$\beta_{Ch,j}$	Choi index
θ	Threshold
$\tilde{\phi}_{macro,j}$	Macro index of j^{th} element
$\beta_{idx,j}$	Damage index value for j^{th} element
N_{opt}	Optimum number of sensors
η_{dev}	Random error of the sensor
η_{linear}	Linearity error of the sensor
η_{max}	Maximum error of the sensor

CHAPTER ONE: INTRODUCTION

1.1 Background

Composites are the combination of two or more type of materials that produce a property in the result product not possessed by the constituent materials (Askeland et al., 2013). They offer a better alternative to traditional materials due to the unique set of properties such as light weight, increased directional strength, high specific strength, corrosion resistance and the ability to tune the mechanical properties as per need (Mukhopadhyay et al., 2021).

Among the different types of composites, fibre-reinforced composites (FRCs) are being increasingly used in a wide range of applications. A typical FMC consists of a matrix and reinforcements. A matrix is a homogenous base material that forms the bulk of the FRCs. The reinforcements are bonded or embedded fibres that are usually responsible for the anisotropy of the composite. According to (Fu & Yao, 2022), FRCs can be classified as:

- Composite laminates,
- Braided composites,
- Woven composites,
- Nanocomposites,
- Sandwich composite, and
- Structural composite.

FRC laminates are the structures built up from multiple layers, called lamina, with same or different orientations. The lamina is a composite material in the form of a sheet, referred to as a layer or a ply. A stack of lamina bonded together in arbitrary directions, by a process of composite lay-up, is a laminate. FRC laminates have some outstanding properties such as low density, high strength, fatigue resistance, high damping properties, fabrication diversity, etc., that has increased their adoption in a wide range of areas.

With the unique set of properties that they exhibit, they are, unfortunately, susceptible to some unique types of defects. Even so, the damages are less well understood in composites as compared to conventional materials (Ghobadi, 2017). These defects adversely affect the integrity and the performance of the composite structures and may even lead to catastrophic failures. The defects in composites could be onset either during the manufacturing process or during the service life.

Manufacturing is crucial in the creation of faults in composite materials, which has a substantial impact on the final product's performance and durability. Manufacturing defects include:

- Inevitable natural defects,
- Formation of voids,
- Presence of contaminants, etc.

One of the most noticeable defects is porosity, which is the production of microscopic spaces or holes in the resin matrix. These gaps might appear as isolated pockets or as interconnected networks, reducing the material's density and mechanical strength. Porosity is frequently the result of suboptimal curing circumstances, such as poor temperature control, pressure disparities during consolidation, or an uneven and quick curing cycle that prevents the resin from entirely flowing into and filling every small crevice. Furthermore, chemical processes during curing might produce gas; if these gases are not properly evacuated before the resin sets, they become trapped and contribute to the formation of voids. Porosity diminishes the composite material's load-bearing capacity and fatigue resistance, making it more prone to environmental degradation because voids allow moisture, chemicals, or other hazardous agents to enter.

Another prevalent flaw in composite materials is the presence of foreign compounds in the matrix. This contamination can arise at several phases of the production process. If the manufacturing environment is not tightly regulated, particles like as dust or fibers from backing sheets may be inadvertently incorporated during the pre-curing stage. These inclusions can also form during the curing process if surfaces are not thoroughly cleaned, leaving residues such as oil fingerprints or other defects. Even after curing, during finishing processes such as trimming or sanding, additional impurities may harm the composite's surface. Such foreign inclusions might break the resin matrix's continuity, potentially lowering bonding strength between layers

and acting as stress concentration spots, resulting in early failure or cracking under load.

Service life flaws relate to the issues that might occur in fiber reinforced resin matrix composites during their operational lifetime, ultimately compromising their performance and durability. Service life defects include:

- Impact loadings (primary cause of defects in composite),
- Delamination effects,
- Matrix cracking,
- Fibre breakage and pull-out.

Resin-rich defects may substantially impact the functionality of composite materials. Micro-sized resin-rich flaws often have modest effects on shear strength and toughness, allowing the composite to retain the majority of its mechanical integrity. However, as the faults reach macro-sized, they can cause stress concentrations that act as focus points for damage, potentially leading to premature material failure. The existence of these larger faults is especially damaging since they diminish the onset strain at which composite failure occurs, undermining the material's overall structural integrity (Fu & Yao, 2022).

Matrix cracking is an important limitation in resin matrix fiber-reinforced composites since it negatively influences their overall performance as well as their mechanical properties by decreasing interlaminar shear strength and compression durability, besides inducing other modes of failure such as delamination. The phenomenon also results mainly from the residual strain in the composite, which is caused by factors such as the thermal expansion difference between the fibers and resin, curing chemical contraction, or processing constraints. Additionally, anisotropic nature of fibers, in conjunction with interactions among constituents of the composite, can lead to large distortions caused by curing, hence paving way to matrix cracking (Fu & Yao, 2022).

Machining defects are an important class of flaws that occur in composite products. Because of their unique composition, composites are prone to machining flaws defined by delamination, tearing, and burr formation. Machining faults in composites are brought about by their innate heterogeneity as well as anisotropic nature, which

leads to random responses toward mechanical loads in different orientations to ultimately generate unreliable performance. Machining processes involve localized employment of large forces in association with high-speed motions of machining cutters, which can cause separation of composite blocks in addition to sudden occurrence of sub-surface delaminations, under cycling load or during secondary machining processes. Such instances not only trigger premature delamination but also induce accelerated deterioration of composite structures with adverse implications to their lifespan. The anisotropic nature of composites makes machining processes particularly demanding. Compared to isotropic products with homogeneous mechanical properties throughout their entirety, composites are such that consideration of various layer or fiber orientations leads to different responses to cutting forces. Such differences can lead to asymmetric formation of the product's surfaces, tearing, or burr formation, with negative consequences to their adhesive bonds between layers, ultimately increasing failure probability in the composite system.

Fiber breakage, which can happen through manufacturing processes or by way of mechanical stresses, severely undermines the load carrying properties of composite materials. Such fiber breakage can happen through overloading, mishandling, or even inherent flaws in fibers; these discontinuities generally induce early failure under load conditions. Fiber rupture results in reductions in overall strength and stiffness of the composite, which in turn causes drastic reductions in performance in addition to reliability.

Fiber pullout is a mechanism where, during mechanical loading, fibers get pulled out from the resin matrix, which is indicative of matrix-fiber interface failure. Such occurrence is often due to poor adhesion of the resin with the fibers, which is more likely to occur due to poor impregnation of the resin during production or poor adhesion in the interface. The presence of such interfacial flaws prevents load transfer from matrix to fibers, causing damage to the structure. In addition, fiber pullout is also considered to be an indicator of failure at an interface with a high tendency to reduce significantly the mechanical properties of the composite structures such as strength, stiffness, and toughness.

Delamination, a type of interfacial defect, is the prominent defect type in composite laminates. Even advanced composite laminates are highly prone to it due to their low inter-ply shear and tensile strengths. (Fu & Yao, 2022) further add that delamination defects are more common in FRC laminates during the manufacturing

process as well. As such, it is very imminent to detect such damages at their earliest to address them and prevent any failure.

There have been many efforts to detect the damage in composite structures with greater precision. Damage detection methods for composite structures can be classified as either global type or local type. Local type damage detection techniques are those that can detect and locate damage in a small area. Conventional non-destructive testing (NDT) techniques such as ultrasonic scanning, X-ray, eddy current, thermography, shearography, etc., are grouped into local type. They have been extensively used for detection of defects in composite laminates in local scale. But if the structure is big and there are multiple possible locations of damage or the defect location is not known, they may not be the ideal choice. That is where global type of damage detection methods such as VBMs come in. They are generally accepted in SHM applications due to their capability to detect and/or locate the defect in large structures (Chaupal & Rajendran, 2023).

VBMs detect the damage based on changes in the dynamic characteristics of the structure such as eigen frequencies (ω_n), mode shapes and damping ratio. Delamination in composite laminates reduces the structural stiffness and thus causes changes in the vibration responses of the laminates (Zhou & Peng, 2022). According to (Chaupal & Rajendran, 2023), VBMs require a lower number of sensors, do not require the prior knowledge of the location of damage, and are easier to perform. They are generally coupled with advanced techniques to get a clearer understanding of the state of the structure and predict and prevent the onset of damage in SHM applications. VBMs generally detect the presence, location and severity of damage using:

- Modal parameters,
- Finite element methods,
- Optimization techniques,
- Signal processing techniques, or
- Machine learning techniques.

A quick review of recent works in this area indicates that VBMs are increasingly being used for damage detection in SHMs. VBMs generally use modal parameters

such as eigen frequencies (ω_n), mode shapes and damping ratio for damage detection. Many past works have taken these parameters to compare the damaged and pristine state of a structure and to detect any possible damage it has. Others have taken it a step further by deriving parameters from these fundamental ones to get a better understanding of the presence, location and extent of damage.

1.2 Problem Statement

With the increasing range of applications of FRC laminates, the detection of any form of damage in them during manufacturing or during service life is very crucial. The defects should be identified in advance to prevent any catastrophic event in the foreseeable future. As such, VBMs can be a better alternative. But VBMs are also affected by the quality of data they receive from the sensors. The number of sensors needed for the task affects the precision of the method. The sensors' accuracy can also introduce bias in the data acquired. To reduce such biases, the number of sensors used might need adjustments. Also, according to (Chaupal & Rajendran, 2023) and (Fu & Yao, 2022), since there is no single consensus in single type of damage detection technique or index, a robust framework that incorporates more than one technique for detecting and evaluating the damage with higher detection efficiency is required, reducing the occurrence of false alarms to a minimum.

1.3 Main Objective

To use vibration-based methods employing modal curvature-based techniques for damage detection of fibreglass reinforced composite beams.

1.4 Specific Objectives

- To fabricate fibreglass reinforced composite laminates and obtain the mechanical properties of the fabricated beams.
- To optimize sensor spacing using a Monte Carlo-based error minimization framework.
- To detect different types of damage using modal curvature-based techniques in a two-stage approach to improve damage localization accuracy.

1.5 Limitations

- The study only considers the first mode of transverse vibration for modal analysis and does not ponder into the effect of higher modes of vibration.
- The effect of material parameters are not studied.

CHAPTER TWO: LITERATURE REVIEW

2.1 Damage in Composites

Common types of damage encountered in composite structures are matrix crack, fibre breakage, fibre-matrix debonding, fibre pull-out, delamination, impact damage, fatigue damage, thermal damage, void formation and buckling or wrinkling (Ghobadi, 2017). On laboratory experiments, these damages can be artificially generated. For example, fibre breakage can be made from fibre cutting before the manufacturing step, delamination can be introduced by inserting Teflon or foreign film between two plies, etc. (Dolbachian et al., 2024). Delamination is the most common type of structural damage in composite structures. It is the separation or splitting between layers of composite material. It is one of the most severe damage types in composite materials. As a result, most researchers have focused on detection of delamination in composite materials (Dolbachian et al., 2024). Main causes of delamination are impact, bending, thermal cycling and manufacturing defects. This leads to a severe reduction in effective transfer of stress between the matrix and fibres, reducing the strength of the composite. Teflon tapes are widely employed to create artificial delamination in composite structures.

2.2 Vibration Based Methods

Conventional techniques such as DIC and Shearography are limited to detecting defects on the surface of the structure and are not ideal for detecting subsurface defects (Ahmed et al., 2021). Among the different VBMs mentioned by (Chaupal & Rajendran, 2023), each have their own shortcomings. Finite element method-based techniques suffer with output variability and can be resource intensive. Also, it requires the development of the model of the actual structure, which might not be always practical (Dolinski & Krawczuk, 2020). Optimization techniques have been garnering popularity in recent years. But these can be complex and difficult to implement efficiently and are often susceptible to numerical noise. Artificial neural network (ANN) and convolution neural network (CNN) based techniques are also increasingly used but they often suffer from requiring substantial amount of training data.

(Chaupal & Rajendran, 2023) further add that signal processing techniques such as Short-Time Fourier Transform (STFT) and Wavelet Transform (WT) also have their own shortcomings which make them unable to be used by themselves to be

used for damage detection. STFT gives constant frequency resolution across the windows because it analyses the complete signal with the same window. Thus, this method is only suitable for quasi-static signals. WT functions well for linear signals and only fails when there is line singularity present or when the signal becomes non-linear. Among modal parameter-based techniques, the techniques that utilize eigen frequencies are limited by low sensitivity and can only detect large damages. Damping ratio based techniques are trickier than eigen frequencies to deal with, making them less reliable for a robust damage detection framework (Jamadar & Kivade, 2017).

2.3 Damage Indices

There are many damage indices (DIs) developed for detecting defect from the change in curvature mode shape. These damage indices can be categorised based on the baseline dependence of the indices as

- Baseline dependent DI
- Baseline free DI.

Damage indices that require a baseline to compare the damaged state to are grouped under baseline dependent DI. Those that do not require a baseline to compare to and can determine the damage from the information of damaged structure only are baseline free DI. They are particularly used for structures with homogenous composition or uniform surface structure. Damage indices can also be classified as:

- Non-normalized DI
- Normalized DI

Non-normalized DI is a direct, physics-based, measure of damage severity used to estimate the damage extent. Such DI is generally directly obtained from, and is related, to stiffness loss or modal parameter changes of the structure due to damage.

Normalized DI is a statistically normalized version of the non-normalized index used to enable damage localization by highlighting outliers in the distribution of damage indices. The statistical normalization is generally performed via Z-score or range normalization. While compiling the values of different damage indices, they are

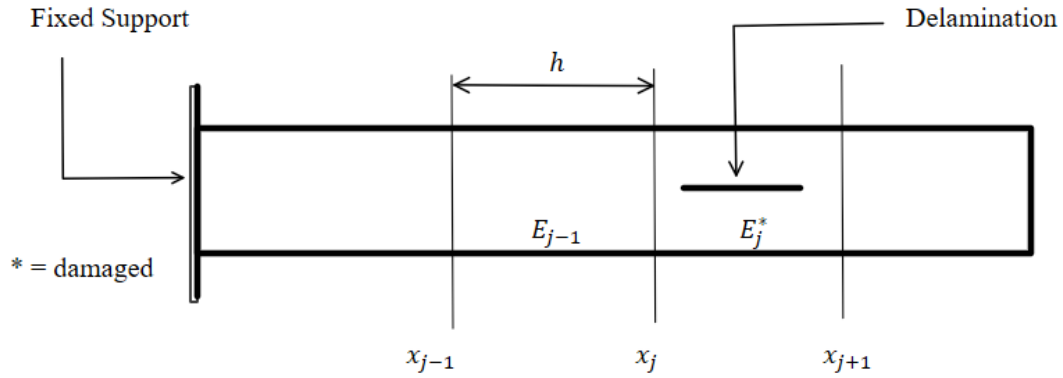

Figure 2.1: A model cantilever beam with delamination

normalized to avoid the over-influence of a single damage index in the compiled macro index.

The use of curvature mode shape for damage detection was introduced by (Pandey et al., 1991). The curvature of a structure was calculated from the mode shape information using central difference as :

$$\kappa_i = \frac{\phi_{i+1} - 2\phi_i + \phi_{i-1}}{l_e^2} \tag{2.1}$$

Over the years, many new damage indices have been defined, each with their unique applications. Due to the scope of the thesis, only baseline dependent methods will be studied. Some prominent ones, as mentioned by (Dessi et al., 2024), are those proposed by (Choi et al., 2005), (Cornwell et al., 1999), (Kim & Stubbs, 2002) and (Stubbs et al., 1995).

It is well known that a mode of vibration possesses some strain energy. The damage in the structure changes the stiffness, and thus the corresponding natural frequency and displacement mode shape that are associated with modal strain energy are also changed.

For a beam with one end fixed, as shown in Figure 2.1, let E_j^* represent an element of the beam with a delamination of length L_d. The strain energy of this element for i^{th} mode is given by:

$$U_j^{(i)} = \frac{1}{2}\int_{x_j}^{x_{j+1}} D(x)\left[\left(\phi^{(i)}(x)\right)''\right]^2 dx = \frac{1}{2}\int_{x_j}^{x_{j+1}} EI(x)\left[\kappa^{(i)}(x)\right]^2 dx \tag{2.2}$$

where,
$\kappa(x,t) = w''(x,t) = \sum_{i=1}^{M} W^{(i)}(t).\kappa^{(i)}(x)$
$\kappa^{(i)}(x) = \left(\phi^{(i)}(x)\right)''$ is the i^{th} modal curvature

For each element, there exists $\bar{D}_j$, such that,

$$U_j^{(i)} = \frac{\bar{D}_j}{2}\int_{x_j}^{x_{j+1}} \left[\kappa^{(i)}(x)\right]^2 dx = \bar{D}_j\gamma_j^i \tag{2.3}$$

As such, damage in a composite structure changes both D_j and $\gamma_j^{(i)}$ of the element. It is also a common knowledge that damage index and the geometry, or rather the curvature, are interrelated as:

$$D_j \propto \left[\kappa^{(i)}(x)\right]^2 \tag{2.4}$$

For the entire beam, the strain energy for i^{th} mode simplifies to :

$$U^{(i)} = \bar{D}\gamma^{(i)} \tag{2.5}$$

The Cornwell Index (Cornwell et al., 1999) quantifies damage by comparing the ratio of local strain energy to global strain energy between damaged and undamaged state. For j^{th} element, it is given by:

$$\beta_{Co,j} = \left(\frac{\gamma_j}{\Gamma_{intact}}\right) / \left(\frac{\gamma_j^*}{\Gamma_{damaged}}\right) \tag{2.6}$$

The Stubbs index introduced by (Stubbs et al., 1995) is a modification of Cornwell index and is expressed as:

$$\beta_{st,j} = \frac{(\gamma_j + \Gamma_{intact})}{(\gamma_j^* + \Gamma_{damaged})} \cdot \frac{\Gamma_{damaged}}{\Gamma_{intact}} \tag{2.7}$$

The index tries to mitigate false positives by balancing local and global energy contributions. (Stubbs et al., 1995) assumed that the local strain energies are negligible as compared to global strain energies.

Cornwell and Stubbs indices are usually expressed as a summation of values over all the modes. The expressions above are for single mode only.

Likewise, (Choi et al., 2005) proposed the Choi Index which employs absolute curvature integrals to detect compliance changes. It is given by:

$$\beta_{\mathrm{Ch},j} = \frac{1 + \left| \int_{x_j}^{x_{j+1}} \kappa(x)\, dx \right|}{1 + \left| \int_{x_j}^{x_{j+1}} \kappa^*(x)\, dx \right|} \tag{2.8}$$

The Choi index evaluates the local curvature of each element. It is suitable for both one dimensional and two dimensional structure and was developed with the aid of concept of compliance.

Cornwell ,Stubbs and Choi indices are non-normalized indices and needs to be normalized before formulating a macro index. The normalization done is generally Z-score based normalization and is given as :

$$B_{idx,j} = \frac{\beta_{idx,j} - \bar{\beta_{idx}}}{\sigma_{\beta_{idx}}} \tag{2.9}$$

After normalization, they can be assembled into a macro index. A macro index (Dessi et al., 2024) combines DIs into a unified metric by using a Z-score normalization:

$$\tilde{\phi}_{macro,j} = \sum \left(\frac{\hat{\beta}_{idx,j} - \mu\hat{\beta}_{idx}}{\sigma\hat{\beta}_{idx}} \right) \tag{2.10}$$

A particular value is flagged as damaged if $\tilde{\phi}_{\mathrm{macro},j} \geq \theta$, where θ is the threshold optimised via ROC analysis.

2.4 Uncertainties

Experimental techniques, such as the ones employed for vibration based damage detection (VBDD), are bound to have some level of uncertainties (Moffat, 1988).

Many studies in the field of VBMs that have previously been conducted have generally glossed over the uncertainties that might arise from conducting the tests in a real-life scenario. The analysis conducted assume that the ability of the algorithm used to avoid false alarm proves the goodness of the method (Dessi et al., 2024).

According to (Yalan et al., 2015), there are generally two sources of uncertainties in measuring modal parameters of a structure. The first one is due to the inherent variability or randomness of the physical and material properties, geometric parameters of the system. Such uncertainties cannot be reduced or eliminated. The second source of uncertainties refer to those arising from measurement noise and the technique used. Such uncertainties can be reduced by precise measurement instruments and improvement in the measuring technique used. For composite structures, there exist much noise due to first source of uncertainties. So, a robust measurement technique is required. Probabilistic approaches are frequently used for handling the uncertainties by treating uncertainties as random variables (Peeters & De Roeck, 2001).

2.5 Monte Carlo Simulation

Statistical techniques based on Monte Carlo Simulation can be employed to establish a confidence limit that takes into account the uncertainties while performing VBDD (Dessi et al., 2024), (Farrar & Jauregui, 1998). Monte Carlo simulation is a computational method that uses repeated random sampling to estimate intricate mathematical quantities or quantify uncertainty in stochastic systems. The method approximates the expected value of a random variable X, defined as

$$\mathbb{E}[X] \approx \frac{1}{N} \sum_{i=1}^{N} x_i \tag{2.11}$$

This approach uses the law of large numbers to ensure the convergence to the true value as $N \to \infty$, with standard error scaling as $\sigma / \sqrt{N}$, with σ as the standard deviation of X. Although initially devised to compute neutron diffusion problems, Monte Carlo techniques are currently being applied across a variety of disciplines including engineering, finance, and physics to model probabilistic events, calculate integrals in high-dimensional cases, and quantify risks in inherently random systems (Rubinstein & Kroese, 2017).

In addition to the MC method, a macro-index based approach that takes into account different DIs that are based on the same technique can form a robust framework for damage detection to reduce false alarms to a minimum (Dessi et al., 2024).

2.6 Singular Value Decomposition

The Singular Value Decomposition (SVD) is a widely used mathematical tool in the field of structural health monitoring (SHM), specifically in modal analysis for precise mode shape extraction from measured vibrations. Experimental observation data are characterized by redundancy, which is unravelled in terms of singular values and singular vectors using SVD, thus allowing the extraction of meaningful modal features while eliminating correlated measurement noises. This inbuilt characteristic makes SVD highly fit for use in operational environments where data usually contain noises and environmental interference (Tian et al., 2023). The efficacy of SVD in retaining structural data while filtering unessential components ensures the resulting mode shapes are reliable inputs in curvature-based approaches used in the detection of damage. Several studies have proved the efficacy of Singular Value Decomposition (SVD) in solving structural damage identification problems. (Liu, 2014) used SVD in diagnosing damage through ultrasonic guided wave signals, highlighting how it can separate damage-induced features from unwanted noises in measurements. This basic principle of distinguishing signal from surrounding noises is specifically applicable when using vibrations in detecting damages in beams, in whose modal curvatures the accurate mode shapes are required. (Tian et al., 2023) further used a modified strategy in identifying internal flaws by complementing Local Mean Decomposition with SVD in a more recent study, thereby highlighting the adaptability of the SVD-based technique in numerous structural arrangements. However, using SVD in retrieving damage-induced signals remains a tremendous concern in composite beam structures, though in their study, they worked with concrete blocks. The use of SVD by modal analysis is a major step in enhancing the accuracy and dependability of mode shape estimations, a vital prerequisite in efficient feature-based damage detection in composite beams.

2.7 Fast Fourier Transform

The FFT is an algorithm that converts time-domain signal to frequency domain thus enabling precise identification of the frequencies that make of the time domain signal. The FFT computes Discrete Fourier Transform (DFT) in an efficient manner by reducing the computation complexity from $O(N^2)$ to $O(N.log(N))$,where N

represents the number of samples as represented in (Cooley & Tukey, 1965):

$$X(f_k) = \sum_{n=0} -i\frac{2\pi kn}{N} \tag{2.12}$$

This allows for spectral analysis in a higher resolution, with frequency resolution $\Delta f = \frac{f_s}{N}$ with f_s representing the sampling rate in Hz. In damage detection scenario, FFT is used to obtain spectral peaks that represent modal frequencies. (Brincker et al., 2001) demonstrated that modal parameters of beam-type structures can be successfully extracted from FFT analysis of ambient vibrations, even in the existence of noise, by utilizing several spectral averages and applying a windowing function, e.g., the Hanning window, to minimize spectral leakage. These methods are used in detecting damage through modal curvature, since accurate modal frequency values are required in estimating curvature profiles from mode shapes (Pandey et al., 1991).

CHAPTER THREE: METHODOLOGY

3.1 Conceptual Framework

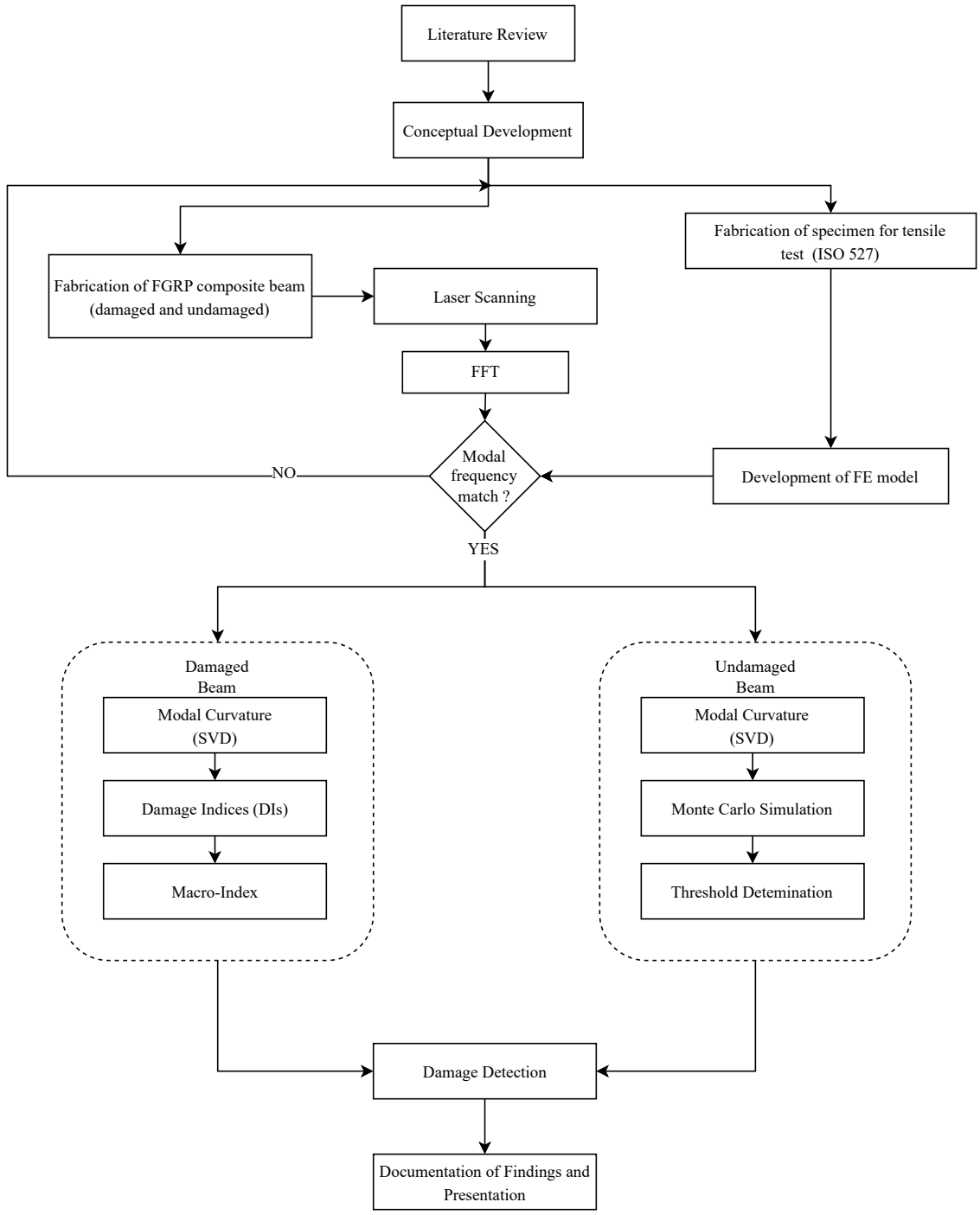

Figure 3.1: Methodology Flowchart

3.2 Fabrication of FGRP beams

Specimens were fabricated using fibreglass (E-glass type) in the form of CSM and as well as plain woven fabric in two different batches. Laminated composite beams were prepared through hand-layup method using three layers of fiberglass CSM of 450 gsm in epoxy resin matrix. The width to thickness ratio was maintained above 10 to minimize shear effects. Specimens were prepared in a single batch to maintain material uniformity and were cured using UV curing.

For the first batch prepared to investigate the effect of location of delamination, the delaminated length was 15 mm and span through the width of the beam. Delamination was introduced at one-third, one-half and two-third of the beam length. The total thickness of the specimens was 3 mm and had a length of 170 mm. Delamination was introduced using Teflon tape was later pried out using GI sheet to prevent any added mass effect it could induce.

For the second batch prepared for investigating the effects of delamination length, the delaminated length was 15 mm and 25 mm and span through the width of the beam. The delamination was introduced at the free end of the one beam and at the centre for another beam. Total thickness each of the specimens was 2 mm and had a length of 120 mm. As in the previous case, the delamination was created using Teflon tape and was removed afterwards.

The mechanical properties were measured according to ISO 527 (Zara et al., 2022) for specimens of each batch (Selver et al., 2018).

3.3 Experimental setup

The test was carried out using microEpsilon scanCONTROL LLT3000-100 laser scanner. It operates based on the principle of optical triangulation, projecting a laser line onto a target surface and using a sensor array to calculate the distance (Z-axis) and position (X-axis) of multiple measuring points. It is used for measuring profiles, lengths, monitoring quality, and checking dimensions. The LLT3000-100 has a specific measuring range with a start of measuring range at 200 mm, a mid of measuring range at 270 mm, and an end of measuring range at 340 mm, with a height of measuring range of 140 mm. The sensor offers high measurement speed and accuracy capable of achieving a profile frequency of up to 10,000 Hz and a resolution of 2,048 points per profile. The data acquired by the sensor can be visualized and

analyzed using software such as scanCONTROL 3D-View, which provides a three-dimensional visualization of the point data. The sensor is also compatible with the LabVIEW instrument driver for scanCONTROL, allowing integration into custom applications. The specifications of the laser scanner are included in appendix A.

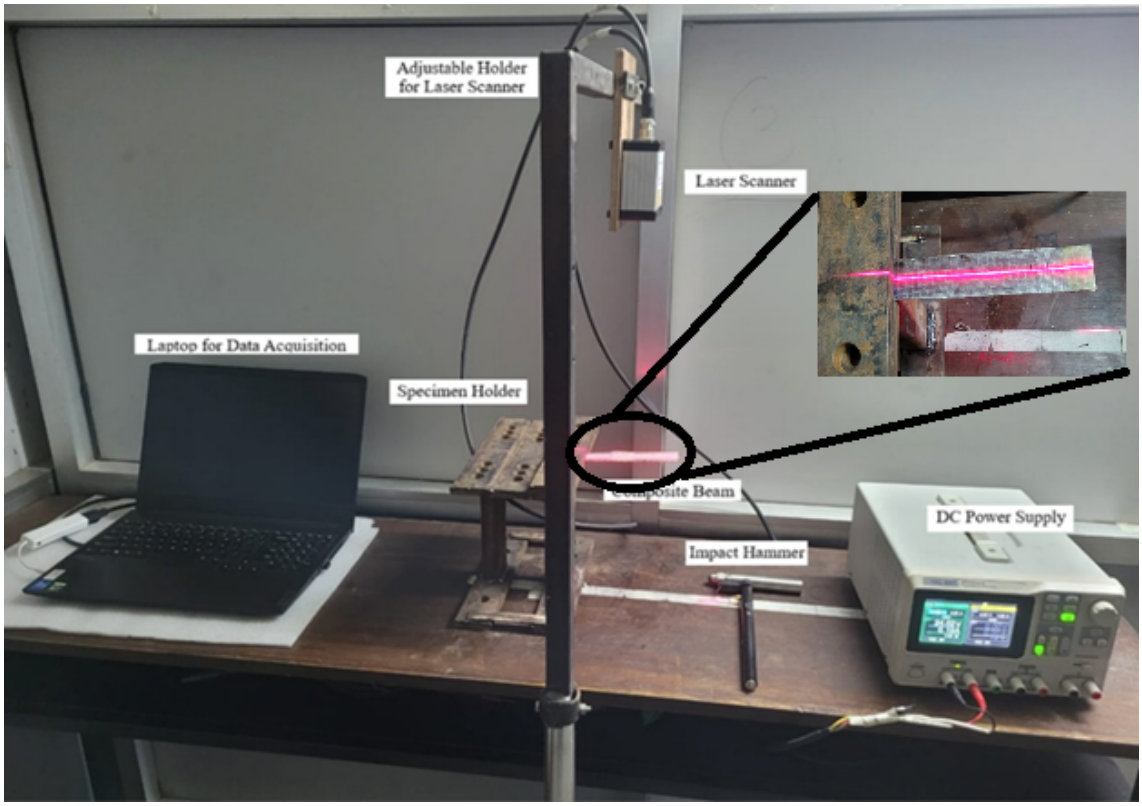

Figure 3.2: New setup layout for data acquisition

For the analysis, the initial idea was to obtain data of each node separately. The setup for that case is as shown in Figure 3.3. Consistency of each such iteration was maintained by giving same initial vertical displacement at the end of the beam. On adopting this method, and the analysis was done by dividing the beam into 4 nodes and 16 nodes separately. However, in each iteration, the nodal data did not show consistency. As a result, the setup shown in Figure 3.2 was used.

As shown in Figure 3.2, the new setup comprises of a composite specimen with its one end fixed, such that it can vibrate in a cantilever configuration. A support arm is used for holding the laser scanner such that it projects a line that extends along the length of the beam and can be used to acquire the displacement information of the beam.

Figure 3.3: Old setup layout for the experiment

The FFT analysis was performed in MATLAB and SVD method was used to extract mode shapes from the displacement data. Each specimen was tested three times, and the average natural frequencies were reported.

A finite element analysis was performed for each damage case to estimate the approximate range of the first modal frequency. A commercial finite element software ANSYS MAPDL was used for FE analysis. The simulations were carried out by employing a higher order 3-D structural solid element (SOLID186) which has 20 nodes and 3 degrees of freedom per node. SOLID186 exhibits quadratic displacement behaviour and is well suited to model object with mesh irregularities. The modal analysis was performed using Block Lanczos algorithm. In MAPDL, the methods available for mode-extraction are Block-Lanczos (LANB), PCG Lanczos (LANPCG), Supernode modal solver (SNODE), Subspace algorithm (SUBSP), Unsymmetric matrix (UNSYM), Damped system (DAMP), Damped system using QR algorithm (QRDAMP) and Variational Technology (VT). For global modal characteristics of a well-conditioned, symmetric system, LANB is more than sufficient. A sample of the code used to perform the analysis is included in Appendix C.

3.4 Sensor layout

For the spacing of sensors, the method outlined by (Dessi et al., 2024) was used. The method outlined in their work related the number of sensors to balancing out

truncation error and bias error. Truncation errors arise form finite difference approximations of the modal curvature. The finite difference is generally central difference, determined from the mode shape values at each node. Smaller element sizes reduce the truncation error but increase experimental complexity. Such errors scale with $O(h^3)$. For first mode, truncation errors are minimal.

Bias errors arise from sensor miscalibration or inaccuracies in its positional location. Larger element sizes reduce bias errors. Bias scales with $O(1/h)$.

For sensor placement, the optimal sensor count is given by:

$$N_{\text{opt}} = \beta_i \left(\frac{1}{2\eta_{\max}} \right)^{1/4} \tag{3.1}$$

For 1st mode of a cantilever beam $\beta_1 = \frac{1.875}{L}$. For the case of the laser scanner, maximum deviation of single point was 0.06% and linearity error of 9 µm. The max deviation represents the random error (95% confidence interval). To estimate the bias contribution:

$$\eta_{\text{dev}} = \frac{0.06\%}{2} = 0.03\% = 0.0003 \tag{3.2}$$

Linearity error is a systematic error and to normalize it, it need to be divided by the maximum expected displacement (ϕ_{max}) of the experiment:

$$\eta_{\text{linear}} = \frac{9, \mu\text{m}}{\phi_{\max}} \tag{3.3}$$

Total bias error is the sum of random and systematic contributions:

$$\eta_{\max} = \eta_{\text{dev}} + \eta_{\text{linear}} \tag{3.4}$$

3.5 Threshold determination and macro index

The Monte Carlo (MC) simulation technique employed here is aimed at statistically accounting for uncertainties due to measurement noise and discretization errors in damage detection. The procedure starts with experimental noise characterization through repeated measurement of the displacement mode shapes of the healthy beam, from which the noise variance $\sigma_j^{(i)}$ is estimated. Synthetic data sets are then created by perturbing analytical mode shapes (found using Euler-Bernoulli beam theory) with Gaussian noise of the same variance determined. For each of N_{trials}

trials, damage indices (Cornwell, Stubbs, and Choi) are calculated for undamaged and synthetically damaged states, where damage is simulated as a local reduction in stiffness. These indices are Z-score normalized to regularize their distributions, then undergo a two-stage process: (1) an agreement condition limits items where all of the normalized indices positively suggest damage, and (2) a macro-index averages these normalized values to yield a composite measure of damage. Statistical analysis of MC results provides confidence intervals for damage severity predictions and position uncertainty. In addition, Receiver Operating Characteristic (ROC) curves are plotted to find the best threshold θ_{opt} that trades off true positive rates (TPR) and false positive rates (FPR).

This framework systematically deals with experimental variability, offering robust thresholds and sensor configurations along with limitations like idealized noise assumptions and homogeneous damage modelling. The result, along with uncertainty bounds and validated thresholds, improves the reliability of curvature-based Structural Health Monitoring (SHM) systems under realistic conditions.

The macro index suggested here is to improve the accuracy of damage detection by combining the information from various damage indices into one value. This improves on the shortcomings of the individual indices, like sensitivity to noise or lack of uniformity between various damage scenarios. An agreement condition filters the elements by demanding that all the normalized indices affirmatively indicate damage and thus removes the false positives by demanding an agreement among indicators. Normalization is achieved by Z-score transformation to provide comparability among indices of varying scales. the threshold of agreement is the threshold that is determined from θ_{opt} , obtained by ROC analysis of Monte Carlo simulations. These simulations generate synthetic data with controlled damage (e.g., stiffness reductions) and Gaussian noise, enabling systematic evaluation of true positive (TPR) and false positive (FPR) rates at different thresholds. The optimal threshold balances detection accuracy and robustness, selected on the basis of measures such as the Youden Index $\mathrm{J} = \mathrm{TPR} - \mathrm{FPR}$.

Only those points where all the indices are above the threshold are flagged as damaged. A limitation of the agreement condition is the strict demand for uniform positivity across indices, which will fail to detect actual damage in the case of partial agreement.

CHAPTER FOUR: RESULTS AND DISCUSSION

4.1 Mechanical Properties and Sample Dimensions

The density and tensile strength of the specimens were tested. The tensile test was performed as per ISO 527 for samples from each batch. The results are presented in Table 4.1 and Table 4.2. Also, Figure 4.1a and Figure 4.1b represent the samples of batch 1 and batch 2 respectively.

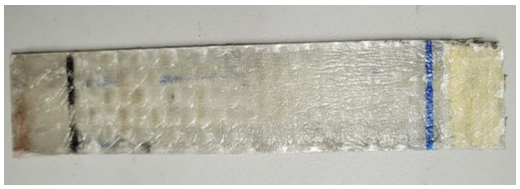

(a) A sample from batch 1

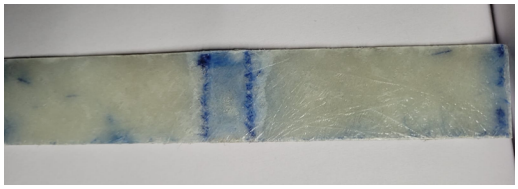

(b) A sample from batch 2

Figure 4.1: Samples from each of the batches prepared

Table 4.1: Material properties of Batch 1 specimen

BATCH 1	
Fabric type used	Bidirectional plain woven
Fabric areal density	600 gsm (0.2 mm thickness)
Fibre volume fraction	0.5
Number of ply layers	2
Density of final specimen	1107.1 kg/m^3
Young's Modulus	5.2 GPa

Table 4.2: Material properties of Batch 2 specimen

BATCH 2	
Fabric type used	Fibreglass chopped strand mat (CSM)
Fabric areal density	450 gsm (0.5 mm thickness)
Fibre volume fraction	0.5
Number of ply layers	3
Density of final specimen	1406.2 kg/m^3
Young's Modulus	3.6 GPa (average of two directions)

For tensile test, sample along only one direction was taken for samples in batch 1 whereas, samples along both directions had to be taken for samples of batch 2. The values obtained for sample 2 were 3516.853333 MPa and 3737.653333 MPa. An average value of 3.6 GPa was taken. For the sample in batch 2, the Young's modulus was 5.2 GPa.

From the samples fabricated, three case setups were prepared:

Case I : 120 mm FRC beam from Batch 1 with edge delamination (eDelam) varied to 15 mm, 25 mm and 35 mm.

Case II : 120 mm FRC beam from Batch 1 with central delamination (cDelam) varied to 15 mm, 25 mm and 35 mm.

Case III : 170 mm FRC beam from Batch 2 with 15 mm delamination, whose position is varied from the free end by $L/3$, $L/2$ and $2L/3$, where L is the beam length.

The dimensions of the samples used and the location of delamination are included in Table 4.3.

Table 4.3: Geometric details of beams considered for analysis

Case	L	δ	x	b	t
I	120 mm	15 mm, 25 mm, 35 mm	Free end	40 mm	2 mm
II	120 mm	15 mm, 25 mm, 35 mm	Free end	40 mm	2 mm
III	170 mm	15 mm	55 mm, 85 mm, 115 mm	40 mm	3 mm

4.2 Data Acquisition

The displacement data was obtained for free vibration of a cantilever configuration of the beam. The scanCONTROL 3D-View 3.8 software was used to obtain the profiles for each case, with the settings as listed in Table 4.4.

Table 4.4: Data acquisition parameters

Exposure time	0.1 ms
Buffered Profiles	150 profiles
Sampling rate	400 Hz
Number of data points	2048

In the current study, the profile frequency of 400 Hz was used, as the scanner showed error while operating above that range. The resolution of 2048 points per profile was utilized. Use of LabVIEW was tried for simultaneously recording the data of impact hammer and laser scanner. Although impact hammer data was recorded in LabVIEW using charge amplifier, issues were encountered with the integration of laser scanner in the LabVIEW. So, this approach was abandoned, and output-only method was used with the help of the scanCONTROL 3D-View 3.8 software. The 3D data was exported in a CSV format and the file consisted of 3 matrices one for X-direction, one for number of buffer profiles, and one for Z-direction. The response along the Z-direction was of concern in this study. The profiles obtained for this particular case are listed in Appendix B.

The data was acquired for each specimen with the parameters of the LLT scanner remaining consistent. For eliminating the effect of surface roughness, the data was acquired for stationary cases and was subtracted from the data at dynamic case. The data thus obtained was again mean normalised.

Initially, different filters such as Butterworth filter, Savitzky-Golay Filter and Gaussian Filter were employed to smooth out the irregularities obtained in the displacement plot in time domain. After thorough consideration, it was found that the surface irregularities were not completely neutralized by the subtracting of stationary data. So, the samples were re-fabricated to obtain a smooth surface using peal ply. The results obtained by smoothing out the surface along which the reading was to be taken were satisfactory and use of any additional filters was avoided.

After obtaining the required time domain data, it was converted to frequency domain by doing FFT analysis in MATLAB. The constituent frequency signals were identified from the FFT plots. Since only first mode vibration was initiated, only one peak frequency peak was obtained.

The first mode frequency for different beams obtained by from experimental and numerical methods are listed in Table 4.5.

Table 4.5: Comparison of natural frequencies obtained from FEM and experiment

Case	**FEM**	**Experiment**	**Error (%)**
I – eDelam	34.003 Hz	33.33 Hz	2.02 %
II – cDelam	35.961 Hz	36.11 Hz	0.41 %
III – L3delam	31.254 Hz	34.67 Hz	9.85 %
III – L2delam	30.962 Hz	29.33 Hz	5.56 %
III – 2L3delam	31.166 Hz	32 Hz	2.61 %

The first-mode natural frequencies from FEM simulations and experiments showed strong agreement for edge-delaminated beams (Table 4.5). For instance, the eDelam15 case exhibited a 1.97% error (34.00 Hz FEM vs. 33.33 Hz experiment), validating the FEM model's accuracy. However, discrepancies arose in L3delam (31.25 Hz FEM vs. 34.67 Hz experiment, 10% error), likely due to imperfect boundary conditions in experiments (e.g., partial clamping slippage) and material inhomogeneity unaccounted for in the homogeneous FEM model. This highlights the need for stochastic material modeling in future simulations to better capture real-world variability.

The range of the laser scanner was sufficient for capturing the entire length of the beam samples from batch 1. For beam samples from batch 2 however, the range of the scanner was not enough. So, only a 120 mm length of the beam was studied from the rigid support, and measurements were taken form the rigid support.

4.3 Sensor Placement

For the 1st mode, the truncation error is always negligible. So, the error is introduced by bias of the sensor used.

For our case, the number of nodes required was obtained as 62. Such a number is primarily due to the smaller length of the specimen fabricated. With the increase in length of the specimen β_i decreases and thus number of nodes required become less.

4.4 Case I

4.4.1 eDelam15

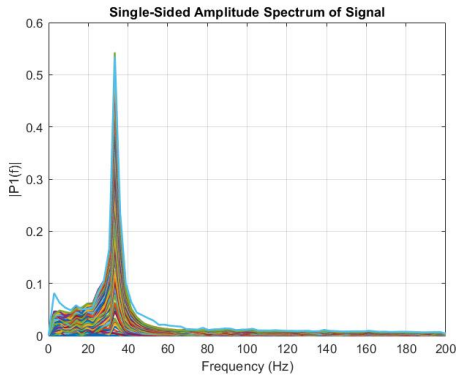

(a) FFT plot of the displacements of different nodes

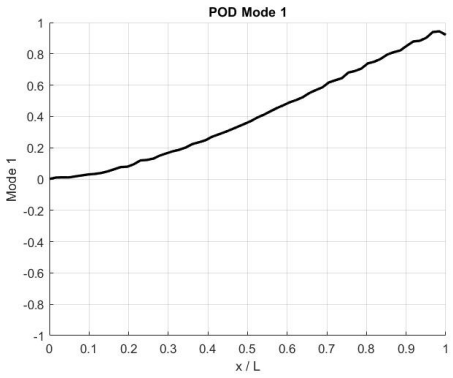

(b) Mode shape for first modal frequency

Figure 4.2: Results for eDelam15 beam

Here, a 15 mm delamination was introduced to the end of the beam. The corresponding FFt plot and mode shapes are included here. A sharp transition is seen at the end of the mode shape curves, even for the undamaged mode. This might be due to the inclusion of the free end in the data acquisition, inducing an unwanted noise.

4.4.2 eDelam 25

Here, a 25 mm delamination was introduced to the end of the beam. The corresponding frequency did not change by a significant amount as compared to the

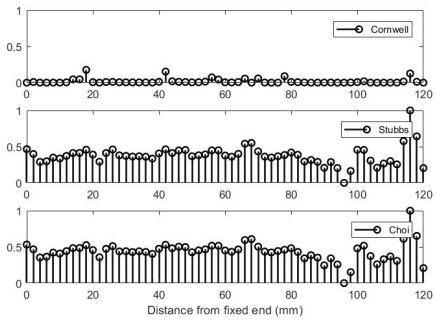

(a) Cornwell, Stubbs and Choi Indices

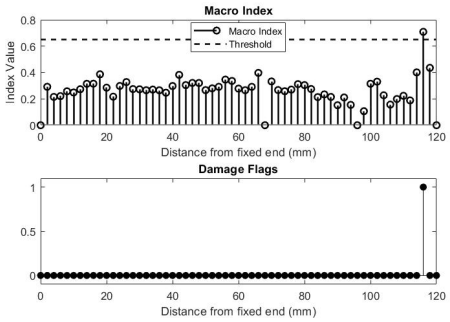

(b) Macro index, threshold and flags

Figure 4.3: Results for eDelam15 beam

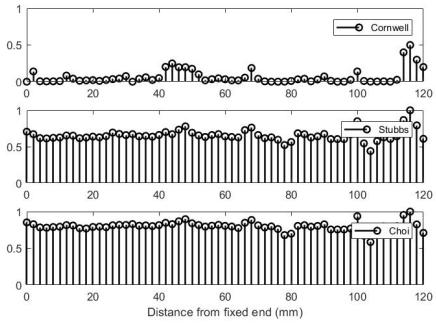

(a) Cornwell, Stubbs and Choi Indices

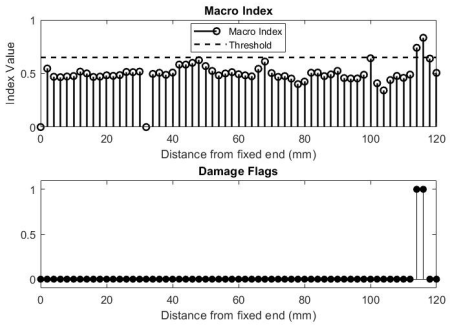

(b) Macro index, threshold and flags

Figure 4.4: Results for eDelam25 beam

eDelam15 case. On the left-hand side graph in Figure 4.4 are plotted the indices of Cornwell, Stubbs, and Choi, showing generally stable readings, although there is one spike in the vicinity of the damage. On the opposite side of the graph, the Macro Index is plotted, which combines these single indices and plots them relative to a threshold value; any readings that fall above this value are classed as indicative of damage, hence the presence of the edge delamination.

4.4.3 eDelam 35

Here, a 35 mm delamination was introduced to the end of the beam (Figure 4.5). In subsection (a), the indices by Cornwell, Stubbs, and Choi are plotted along the length of the beam, from the fixed end, exhibiting localized oscillations with significant changes near the 120 mm mark, which might reflect potential damage. Even if the Cornwell index gets closer to the zero threshold value, both Stubbs and Choi indices show greater decreases towards the free end of the beam, which may reflect the presence of delamination. In subsection (b), the Macro Index is plotted together with a red dashed threshold value; any value exceeding this threshold indicates the

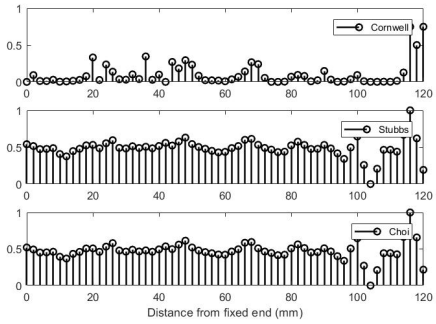

(a) Cornwell, Stubbs and Choi Indices

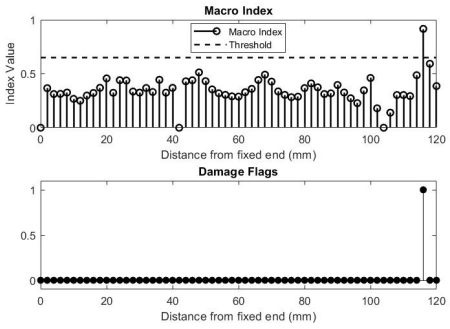

(b) Macro index, threshold and flags

Figure 4.5: Results for eDelam35 beam

presence of damage. An evident peak in the Macro Index is also evident near the 120 mm location, which is also reflected by a red flag in the corresponding lower plot, thus verifying the detection of damage. Overall, all these indices and plots validate the presence of damage near the free end of the beam.

4.5 Case II

4.5.1 cDelam 15

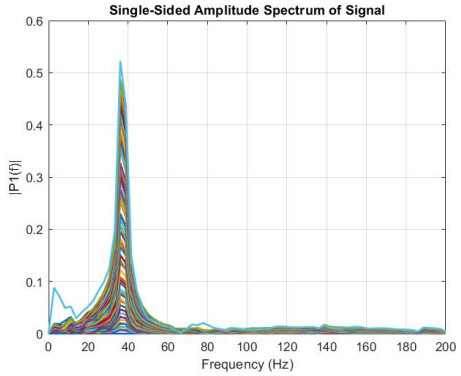

(a) FFT plot of the displacements of different nodes

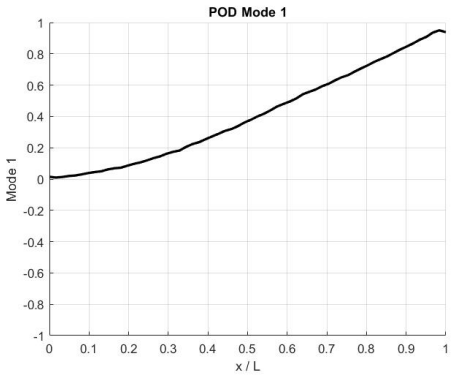

(b) Mode shape for first modal frequency

Figure 4.6: Results for eDelam15 beam

Figure 4.7 shows the results for the cDelam15 beam, which is defined by a delamination of 15 mm in length located near the midpoint of the beam. In subsection (a), the Cornwell, Stubbs, and Choi-developed indices are plotted along the length of the beam, each of which features significant peaks that correlate to the locus of introduced damage. These significant peaks in index value reflect high levels of sensitivity of the indices to structural changes caused by delamination. Subsection (b) plots the Macro Index against a red dashed threshold curve, together with the

associated damage indicators. An interesting spike in the Macro Index is visible near the 60 mm location—also near the beam's midpoint—far beyond the threshold and leading to a single red flag in the lower plot.

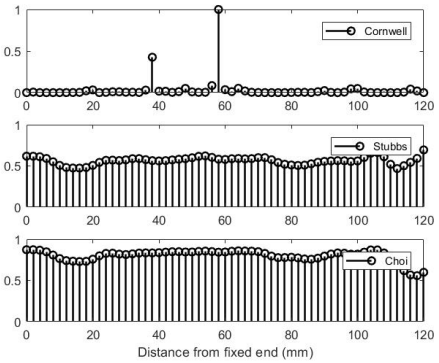

(a) Cornwell, Stubbs and Choi Indices

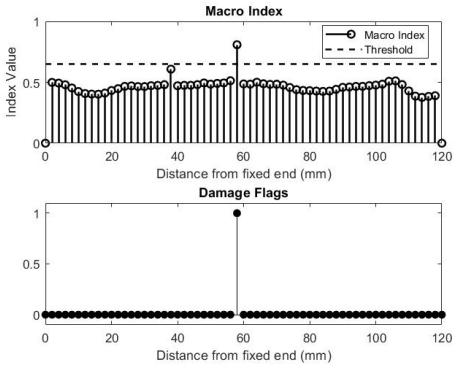

(b) Macro index, threshold and flags

Figure 4.7: Results for cDelam15 beam

4.5.2 cDelam 25

Figure 4.8 shows three individual indices—Cornwell, Stubbs, and Choi—used for locating a 25 mm delamination near the center of the beam. Each index is plotted in terms of the length of the beam relative to the fixed end, making the identification of damage easy. To the left, the corresponding indexes show relatively low magnitudes across the beam, having a localized peak near the location of the delamination. To the right, the Macro Index—a combination of these three indexes—is plotted together with a threshold curve; magnitudes above this curve are emphasized, roughly outlining the damaged area.

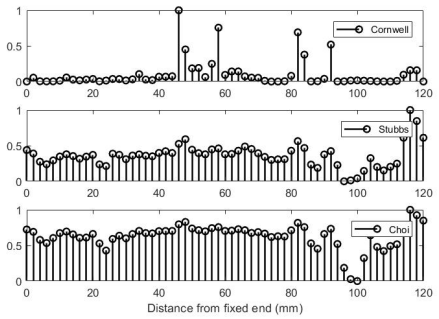

(a) Cornwell, Stubbs and Choi Indices

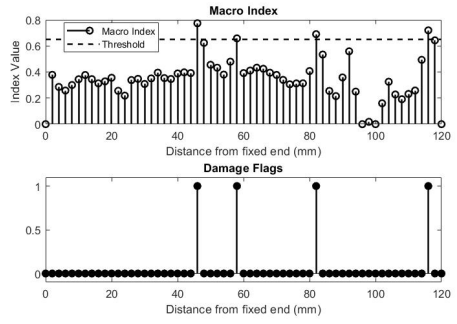

(b) Macro index, threshold and flags

Figure 4.8: Results for cDelam25 beam

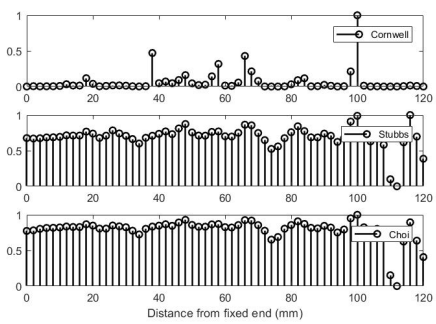

(a) Cornwell, Stubbs and Choi Indices

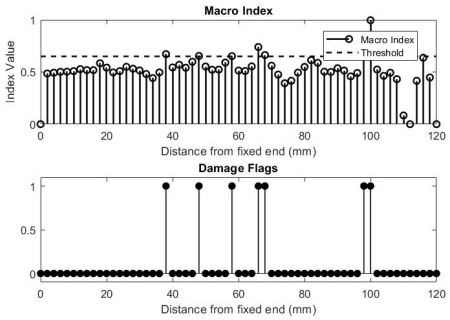

(b) Macro index, threshold and flags

Figure 4.9: Results for cDelam35 beam

4.5.3 cDelam 35

Here, a 35 mm delamination was introduced to the center of the beam (4.9). In subsection (a), the metrics proposed by Cornwell, Stubbs, and Choi all exhibit multiple peaks along the length of the beam, notably at the mid-span and in the vicinity of the free end, denoting locations at which a noticeable change in structural response is observed due to damage. In contrast to isolated spikes, the presence of multiple major disturbances across all three indices suggests a more complex or distributed damage pattern. This claim is additionally supported in subsection (b) by the Macro Index, which is seen to have the threshold line exceeded at multiple points—most notably at the 40 mm, 60 mm, and 80 mm intervals. The damage flags shown in the lower plot register precisely with these peaks, suggesting the presence of three possible damage zones. Only the middle spike represents the actual location of the damage.

4.6 Case III

In the third case, the location of the delamination was varied along the length of the beam. The experimental frequency ranges obtained for first mode vibration for different cases are given in Figure 4.10.

4.6.1 L3delam

Here, a 15 mm delamination was introduced at a 55 mm distance from the fixed end of the beam. Despite the noises present, the framework was able predict the exact delamination location of the beam.

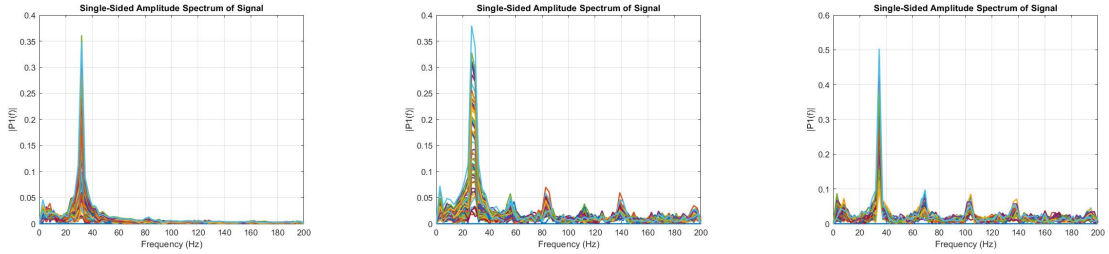

(a) FFt plot for 2L3delam (b) FFt plot for L2delam (c) FFt plot for L3delam

Figure 4.10: FFT plots for specimen of batch2 with variation of delamination location

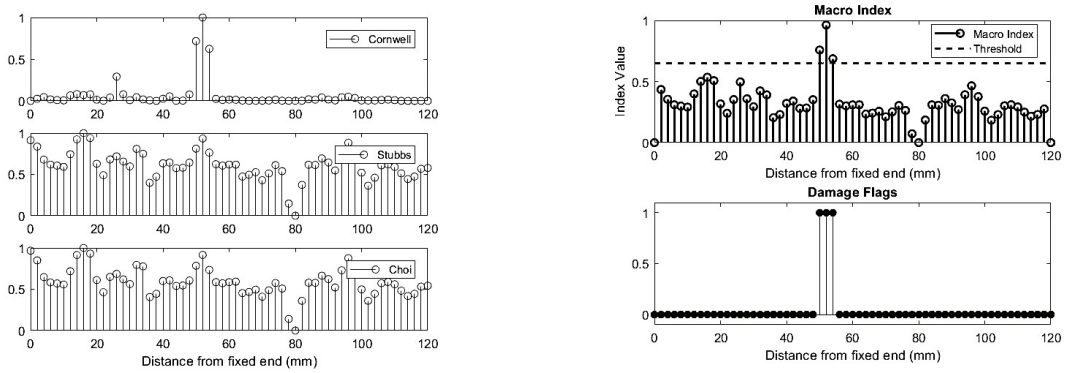

(a) Cornwell, Stubbs and Choi Indices (b) Macro index, threshold and flags

Figure 4.11: Results for L3delam beam

4.6.2 L2delam

Here, a 15 mm delamination was introduced at a 85 mm distance from the fixed end of the beam.In part (a), the Cornwell, Stubbs, and Choi indices show visible responses, specifically around the region 85 mm. The Stubbs and Choi indices show gradual builds and big peaks in the region, while the Cornwell index shows a drastic spike, which is in concordance with a sensitive indication of the localized damage. Part (b) also bears witness to this observation from the Macro Index plot, where multiple values cross the red threshold line—particularly around 85 mm—indicating areas of interest. The lower damage flag plot bears witness to this with open red markers, like one at around 85 mm, confirming successful detection and localization of the delamination. The presence of additional flags suggests some sensitivity to nearby structural variations, but the primary damage site is properly located.

4.6.3 2L3delam

Here, a 15 mm delamination was introduced at a 115 mm distance from the fixed end of the beam. Part (a) illustrates through the Cornwell, Stubbs, and Choi indices

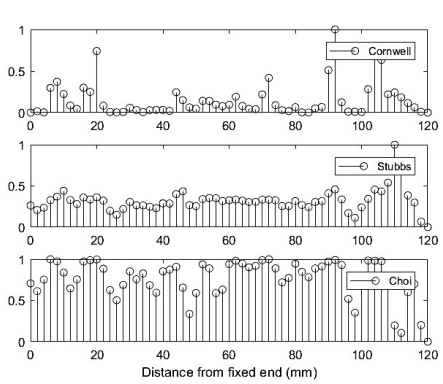

(a) Cornwell, Stubbs and Choi Indices

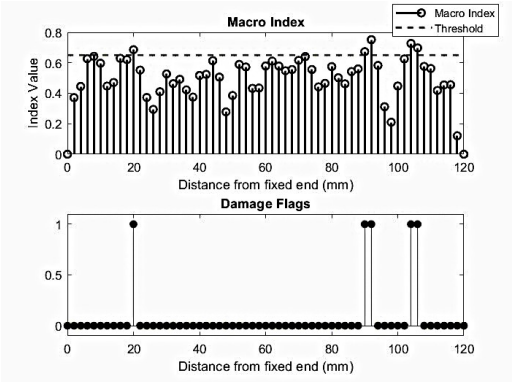

(b) Macro index, threshold and flags

Figure 4.12: Results for L2delam beam

a clear spike near the free end of the beam at around location 115 mm, to be expected from the damage introduced. While all three indices offer oscillations along the beam, the largest disturbances occur around the damaged area, especially in the instance of the Cornwell index, which offers a clear peak. In part (b), the Macro Index plot indicates that the damage is correctly detected by crossing the red threshold line at the correct position. The corresponding damage flag plot also confirms this with one red flag around 115 mm, which is correct localization of the delamination.

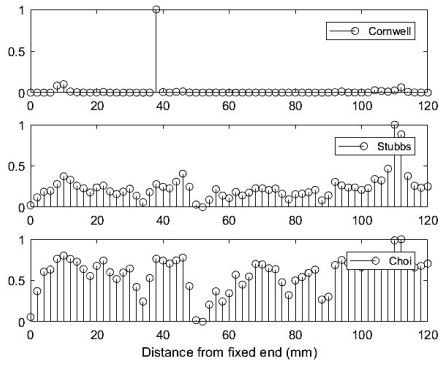

(a) Cornwell, Stubbs and Choi Indices

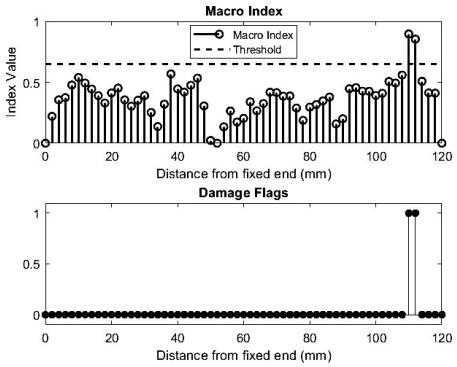

(b) Macro index, threshold and flags

Figure 4.13: Results for 2L3delam beam

CHAPTER FIVE: CONCLUSIONS AND RECOMMENDATIONS

5.1 Conclusion

Techniques involving the use of curvature for damage detection in composite beams show potential as a result of their greater sensitivity to localized stiffness reductions caused by damage. These methods, however, may not always provide reliable estimates of damage in all cases. Measurement errors, boundary condition variations, and mode shape quality can affect unfavorably the reliability of curvature measurements.

Integrating the methods based on curvature with other damage-sensitive indicators, like strain energy-based indicators, modal flexibility-based indicators, or frequency variations, in the form of a composite or macro damage index, enhances the reliability and accuracy of damage detection. It also allows cross-validation of diverse indicators and decreases the possibility of spurious identification of damage, while improving spatial resolution in the identification of damage.

In addition, damage detection system efficacy can be improved by determining statistically significant damage thresholds. Here, Monte Carlo simulations come in as a pivotal tool, enabling the creation of many scenarios that reflect uncertainties in system parameters as well as measurement noise. These simulations support the creation of reliable cutoff thresholds in damage detection, thus improving the level of confidence in detection results under various conditions.

In summary, while curvature-based analysis methods have specific shortcomings when used in standalone form, their performance can be greatly enhanced by the combination of various indexes in conjunction with the application of probabilistic thresholding methods based on Monte Carlo simulation. Overall, this integrated approach provides a strong, reliable tool for damage detection and location in composite beam structures.

5.2 Recommendations

1. **Utilization of High-Order Vibrational Modes**
   Exclusive use of the first bending mode can lead to overlooking damage features that manifest themselves predominantly at higher frequencies or that have torsional nature. Incorporation of second and third bending modes, as well as

torsional or coupled bending–torsion modes, greatly improves the spatial resolution and noise immunity of the damage indicator. A multi-modal curvature index—developed through systematic weighting of curvature changes across a number of modes—promises to detect a wider range of damage patterns and to reduce the possibility of false negatives, especially in cases where an individual mode can be insensitive to the location or size of a particular defect.

2. **Expansion to Intricate Geometries**
   The modal curvature-based framework, originally developed for prismatic composite beams, can be duly extended to include members having curved or non-uniform cross-sectional geometries. The complex geometric features of pipes, pressure vessels, and doubly curved panels can be dealt with by extending the curvature extraction method to curvilinear coordinate systems. Numerical verification by simulations based on finite element models of cylindrical shells and free-form structures has to be carried out before implementation to ensure that localization accuracy and damage sensitivity are still preserved at high levels, even when the geometric features deviate considerably from those of straight beams.

3. **Application to Various Damage Mechanisms**
   Though this study focuses mainly on transverse fractures and delaminations, composite materials are susceptible to a wide range of damage types, such as fiber breakage, matrix microcracking, barely visible impact damage, and environmental degradation. Extension of the macro index approach to address these mechanisms requires re-examination of threshold criteria and perhaps the introduction of other dynamic quantities—e.g., changes in damping ratios or natural frequency shifts—to discern among different damage modes. These refinements will broaden the usefulness of the method across components in the aerospace, automotive, and civil infrastructure industries.

4. **Integration of Material Inhomogeneity**
   The use of the assumption of uniform laminate material properties in analytical tools is convenient, yet it ignores the inherent variability in fiber volume fraction, ply orientation, and behavior of the interface. Later studies need to use stochastic distributions of materials in both finite element analyses and Monte Carlo-based thresholding methods. Through the simulation of true heterogeneity at the ply level and incorporation of measurement noise, it is possible to compare their effects on curvature sensitivities and false alarm rates

and thus optimize damage thresholds and enhance the reliability of composite material detection systems in real applications.

REFERENCES

Ahmed, O., Wang, X., Tran, M.-V., & Ismadi, M.-Z. (2021). Advancements in fiber-reinforced polymer composite materials damage detection methods: Towards achieving energy-efficient SHM systems. *Composites Part B: Engineering*, *223*, 109136. https://doi.org/10.1016/j.compositesb.2021.109136

Askeland, D. R., Haddleton, F., Green, P., & Robertson, H. (2013, November). *The Science and Engineering of Materials*. Springer.

Brincker, R., Zhang, L., & Andersen, P. (2001). Modal identification of output-only systems using frequency domain decomposition. *Smart Mater. Struct.*, *10*(3), 441. https://doi.org/10.1088/0964-1726/10/3/303

Chaupal, P., & Rajendran, P. (2023). A review on recent developments in vibration-based damage identification methods for laminated composite structures: 2010–2022. *Composite Structures*, *311*, 116809. https://doi.org/10.1016/j.compstruct.2023.116809

Choi, S., Park, S., Yoon, S., & Stubbs, N. (2005). Nondestructive damage identification in plate structures using changes in modal compliance. *NDT E International*, *38*(7), 529–540. https://doi.org/10.1016/j.ndteint.2005.01.007

Cooley, J. W., & Tukey, J. W. (1965). An algorithm for the machine calculation of complex Fourier series. *Math. Comp.*, *19*(90), 297–301. https://doi.org/10.1090/S0025-5718-1965-0178586-1

Cornwell, P., Doebling, S. W., & Farrar, C. R. (1999). APPLICATION OF THE STRAIN ENERGY DAMAGE DETECTION METHOD TO PLATE-LIKE STRUCTURES. *Journal of Sound and Vibration*, *224*(2), 359–374. https://doi.org/10.1006/jsvi.1999.2163

Dessi, D., Passacantilli, F., & Venturi, A. (2024). Analysis and mitigation of uncertainties in damage identification by modal-curvature based methods. *Journal of Sound and Vibration*, *596*, 118769. https://doi.org/10.1016/j.jsv.2024.118769

Dolbachian, L., Harizi, W., & Aboura, Z. (2024). Experimental Linear and Nonlinear Vibration Methods for the Structural Health Monitoring (SHM) of Polymer-Matrix Composites (PMCs): A Literature Review. *Vibration*, *7*(1), 281–325. https://doi.org/10.3390/vibration7010015

Dolinski, L., & Krawczuk, M. (2020). Analysis of modal parameters using a statistical approach for condition monitoring of the wind turbine blade. *Applied Sciences*, *10*(17), 5878. https://doi.org/10.3390/app10175878

Farrar, C. R., & Jauregui, D. A. (1998). Comparative study of damage identification algorithms applied to a bridge: I. Experiment. *Smart Mater. Struct.*, *7*(5), 704–719. https://doi.org/10.1088/0964-1726/7/5/013

Fu, Y., & Yao, X. (2022). A review on manufacturing defects and their detection of fiber reinforced resin matrix composites. *Composites Part C: Open Access*, *8*, 100276. https://doi.org/10.1016/j.jcomc.2022.100276

Ghobadi, A. (2017). Common Type of Damages in Composites and Their Inspections. *World Journal of Mechanics*, *7*(2), 24–33. https://doi.org/10.4236/wjm.2017.72003

Jamadar, N. I., & Kivade, S. B. (2017). Detection of Internal Delamination in Composite Mono Leaf Spring based on Vibration Characteristics. *Journal of The Institution of Engineers (India) Series C*, *100*(1), 23–35. https://doi.org/10.1007/s40032-017-0374-x

Kim, J.-T., & Stubbs, N. (2002). Improved damage identification method based on modal information. *Journal of Sound and Vibration*, 223–238. https://doi.org/10.1006/jsvi.2001.3749

Liu, C. (2014, August). *Singular Value Decomposition Applied to Damage Diagnosis for Ultrasonic Guided Wave Structural Health Monitoring* [thesis]. Carnegie Mellon University. https://kilthub.cmu.edu/articles/thesis/Singular_Value_Decomposition_Applied_to_Damage_Diagnosis_for_Ultrasonic_Guided_Wave_Structural_Health_Monitoring/6722909/1

Moffat, R. J. (1988). Describing the uncertainties in experimental results. *Experimental Thermal and Fluid Science*, *1*(1), 3–17. https://doi.org/10.1016/0894-1777(88)90043-X

Mukhopadhyay, T., Naskar, S., Chakraborty, S., Karsh, P. K., Choudhury, R., & Dey, S. (2021). Stochastic Oblique Impact on Composite Laminates: A Concise Review and Characterization of the Essence of Hybrid Machine Learning Algorithms. *Arch Computat Methods Eng*, *28*(3), 1731–1760. https://doi.org/10.1007/s11831-020-09438-w

Pandey, A., Biswas, M., & Samman, M. (1991). Damage detection from changes in curvature mode shapes. *Journal of Sound and Vibration*, *145*(2), 321–332. https://doi.org/10.1016/0022-460X(91)90595-B

Peeters, B., & De Roeck, G. (2001). One-year monitoring of the Z24-Bridge: Environmental effects versus damage events. *Earthquake Engineering Structural Dynamics*, *30*(2), 149–171. https://doi.org/10.1002/1096-9845(200102)30:2<149::AID-EQE1>3.0.CO;2-Z

Rubinstein, R. Y., & Kroese, D. P. (2017). *Simulation and the Monte Carlo method* (Third edition). Wiley.

Selver, E., Ucar, N., & Gulmez, T. (2018). Effect of stacking sequence on tensile, flexural and thermomechanical properties of hybrid flax/glass and jute/glass thermoset composites. *Journal of Industrial Textiles*, *48*(2), 494–520. https://doi.org/10.1177/1528083717736102

Stubbs, N., Kim, J.-T., & Farrar, C. (1995). Field Verification of a Nondestructive Damage Localization and Severity Estimation Algorithm. *Proc SPIE*, *2460*, 210.

Tian, X., Ao, J., Ma, Z., Ma, C., & Shi, J. (2023). An Internal Defect Detection Algorithm for Concrete Blocks Based on Local Mean Decomposition-Singular Value Decomposition and Weighted Spatial-Spectral Entropy. *Entropy*, *25*(7), 1034. https://doi.org/10.3390/e25071034

Yalan, X., Qian, Y., Chen, J., & Song, G. (2015). Probability-based damage detection using model updating with efficient uncertainty propagation. *Mechanical Systems and Signal Processing*, *60-61*, 958–970. https://doi.org/10.1016/j.ymssp.2014.11.008

Zara, A., Belaidi, I., Khatir, S., Brahim, A. O., Boutchicha, D., & Wahab, M. A. (2022). Damage detection in GFRP composite structures by improved artificial neural network using new optimization techniques. *Composite Structures*, *305*, 116475. https://doi.org/10.1016/j.compstruct.2022.116475

Zhou, T., & Peng, Y. (2022). Efficient reliability analysis based on deep learning-enhanced surrogate modelling and probability density evolution method. *Mechanical Systems and Signal Processing*, *162*, 108064. https://doi.org/10.1016/j.ymssp.2021.108064

APPENDIX A: LASER SCANNER SPECIFICATIONS

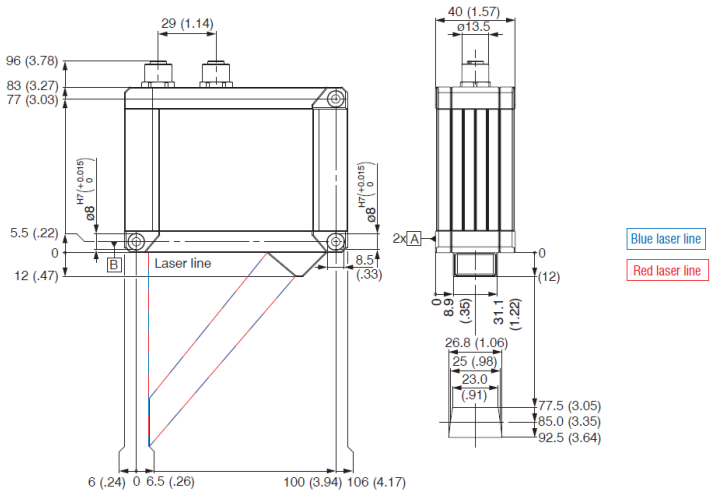

Figure A.1: microEpsilon scanCONTROL LLT3000-100 laser scanner

Table A.1: Measurement range details

Measuring range	Absolute distance (z)	Width (x)
Beginning	200 mm	79.6 mm
Midrange	270 mm	104.8 mm
End	340 mm	130.2 mm

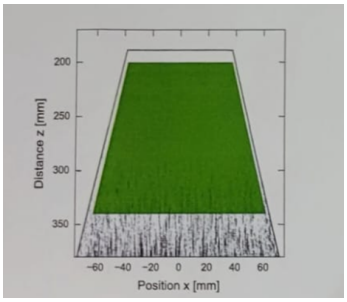

Figure A.2: Laser scanner measuring range

APPENDIX B: SAMPLE MATLAB CODE

DelaminationDetection.m

```
%% Preamble
close all;
clear;
clc;

% Define parameters and file names
folder   = '0000000000000000000000000000000 04-03\cDelam15Def
    ';
% folder = '03-28\2L3';
trial    = '14';
delam    = 'cDelam15Def';
nNodes   = 62;          % Number of nodes to take
Fs       = 400;         % Sampling Frequency (Hz)

% Construct file names using fullfile for platform
    independence
stFile   = fullfile(folder, [trial, delam, 'St', '.csv']);
oscFile  = fullfile(folder, [trial, delam, 'Osc', '.csv']);
opFile   = fullfile(folder, [trial, delam, num2str(nNodes), '.
    xlsx']);

%% Data Picker - nNodes points
funDataPicker(stFile, oscFile, opFile, nNodes);

%% Cleaning the Data
data = xlsread(opFile);
df = data - mean(data);
df = df / max(df(:));
df = df - df(:,1);

filteredName = fullfile(folder, [trial, delam, num2str(nNodes
    ), 'filtered.xlsx']);

%% FFT Plot
bufferProfiles = size(df, 1);
t = (0:(bufferProfiles - 1)) / Fs;
```

```
FFTnatFreq = FFTplotter(df, Fs);
% filteredData = butterFilter(df,Fs,FFTnatFreq,.5,4);
% figure
% FFTplotter(filteredData, Fs);


filteredData = zeros(size(df));
%
for i=1:nNodes
    filteredData(:,i) = sgolayfilt(df(:,i), 3, 11); % 3rd-
        order, 11-point window
end
figure
FFTplotter(filteredData, Fs);
% filteredData = df;
%% PSD
% figure
%  for i=1:nNodes
%      periodogram(filteredData(:,i),rectwin(bufferProfiles),
    bufferProfiles,Fs,'psd');
%      hold on;
%  end
% grid on; legend show; hold off;
%% Plotting Response of Each Node
peakingTime = funPlotter(filteredData, Fs);

%% Mode Shapes SVD
MS = abs(modeShapeSVDmodif(filteredData));

%% Curvature Calculation and Gapped Smoothing
dx = 120 / (nNodes - 1);
curvature = computeCurvature(MS, dx);

% Appllication of Gapped Smoothing Method (GSM)
gap = 3; % Define gap size
smoothed_curvature = GSM(curvature, gap);

% Use of absolute mode shapes for further analysis
MS = abs(MS);

```

```
% Plot of original and smoothed curvature
figure;
% stem(1:nNodes, curvature, 'LineWidth', 1.5, 'Color', 'k');
hold on;
 stem(1:nNodes, smoothed_curvature, 'LineWidth', 1.5, 'Color'
    , 'r');
title('Modal Curvature');
xlabel('Node');
xlim([1 nNodes]);
% legend('Original Curvature', 'Smoothed Curvature');

%% Intact beam Data
% Loading intact beam data
IntactFolder  = '0000000000000000000000000000000 04-03';
% IntactFolder = '03-28\ud';
Itrial = '';
% Construction of file names using fullfile for platform
   independence
IstFile  = fullfile(IntactFolder, [Itrial, 'udDef', 'St', '.
   csv']);
% IstFile  = fullfile(IntactFolder, [Itrial, 'ud', 'St', '.
   csv']);
IoscFile = fullfile(IntactFolder, [Itrial, 'udDef', 'Osc', '.
   csv']);
IopFile  = fullfile(IntactFolder, [Itrial, 'udDef', num2str(
   nNodes), '.xlsx']);

funDataPicker(IstFile, IoscFile, IopFile, nNodes);

intactFile = fullfile(IntactFolder,[Itrial, 'udDef', num2str(
   nNodes), '.xlsx']);
data_intact = xlsread(intactFile); % Intact mode shapes
intactDataFiltered = data_intact - mean(data_intact);
intactDataFiltered = intactDataFiltered / max(
   intactDataFiltered(:));
intactDataFiltered = intactDataFiltered - intactDataFiltered
   (:,1);

MS_intact = modeShapeSVDmodif(intactDataFiltered);

```

```
%% Threshold Determination

% Determination of optimal threshold
theta_opt = determine_threshold(MS_intact', dx, 'N_mc', 1000, 'confidence', 0.85);

%% Curvature Difference Calculation
% MS_ud = modeShapeCantilever(nNodes)';
curvature_ud = computeCurvature(MS_intact, dx);
curvatureDiff = curvature - curvature_ud;

% Normalization of curvature difference
NcurvatureDiff = (curvatureDiff - min(curvatureDiff)) / (max(curvatureDiff) - min(curvatureDiff));

figure;
stem(1:nNodes, curvatureDiff, 'LineWidth', 1.5, 'Color', 'b');
hold on;
stem(1:nNodes, abs(curvatureDiff), 'LineWidth', 1.5, 'Color', 'r');

%% Damage Indices Plot
Conwell = compute_cornwell_index(MS_intact, MS, dx)';
Stubbs  = compute_stubbs_index(MS_intact, MS, dx)';
Choi    = compute_choi_index(MS_intact, MS, dx)';

% subplot(3,1,1)
% stem(linspace(0,120,nNodes-1), Conwell, 'DisplayName', 'Cornwell');
% subplot(3,1,2)
% stem(linspace(0,120,nNodes-1), Stubbs, 'DisplayName', 'Stubbs');
% subplot(3,1,3)
% stem(linspace(0,120,nNodes-1), Choi, 'DisplayName', 'Choi');
% legend;
% xlabel('Distance from fixed end (mm)');


```

```
135
136 %% Macro Index Calculation
137 % normalized indices
138 [norm_Cornwell, norm_Stubbs, norm_Choi] = deal(...
139     (Conwell-mean(Conwell))/std(Conwell), ...
140     (Stubbs-mean(Stubbs))/std(Stubbs), ...
141     (Choi-mean(Choi))/std(Choi));
142
143 norm_Cornwell = (norm_Cornwell - min(norm_Cornwell))/(max(
    norm_Cornwell)-min(norm_Cornwell));
144 norm_Stubbs = (norm_Stubbs - min(norm_Stubbs))/(max(
    norm_Stubbs)-min(norm_Stubbs));
145 norm_Choi = (norm_Choi - min(norm_Choi))/(max(norm_Choi)-min(
    norm_Choi));
146
147
148 subplot(3,1,1)
149 stem(linspace(0,120,nNodes-1), norm_Cornwell, 'DisplayName',
    'Cornwell');legend;
150 subplot(3,1,2)
151 stem(linspace(0,120,nNodes-1), norm_Stubbs, 'DisplayName', '
    Stubbs');legend;
152 subplot(3,1,3)
153 stem(linspace(0,120,nNodes-1), norm_Choi, 'DisplayName', '
    Choi');
154 legend;
155 xlabel('Distance from fixed end (mm)');
156 theta_opt = 0.65;
157
158
159 % macro index and damage flags
160 [macro_idx, damage_flags] = compute_macro_index_weighed(
    norm_Cornwell, norm_Stubbs, norm_Choi, theta_opt);
161
162 %% Plotting DI results
163 figure;
164 subplot(2,1,1);
165 stem(linspace(0,120,nNodes-1), macro_idx, 'b', 'LineWidth',
    1.5);
166 hold on;
```

```
167
168 plot([0,120], [theta_opt, theta_opt], '--r', 'LineWidth',
        1.5);
169 title('Macro Index'); xlabel('Distance from fixed end (mm)');
        ylabel('Index Value');
170 legend('Macro Index', 'Threshold', 'Location', 'best');
171
172 subplot(2,1,2);
173 stem(linspace(0,120,nNodes-1),damage_flags, 'filled', 'Color'
        , 'r');
174 title('Damage Flags'); xlabel('Distance from fixed end (mm)')
        ; ylim([-0.1 1.1]);
175
176 %% Curvature Data to Excel
177 Nfolder    = '0000000000000000000000000000000 04-03';
178 op         = fullfile(Nfolder, [num2str(nNodes), 'Curvature.
        xlsx']);
179 sheetName = [trial, delam];
180 % xlswrite(op, curvature, sheetName);
181
182 %% Function Definitions
183
184 function curvature = computeCurvature(MS, dx)
185     % Compute curvature using finite difference
            approximations.
186     n = length(MS);
187     curvature = zeros(n, 1);
188
189     % Central difference for interior points
190     curvature(2:end-1) = diff(MS, 2) / dx^2;
191
192     % Forward difference for first point
193     curvature(1) = (2*MS(1) - 5*MS(2) + 4*MS(3) - MS(4)) / dx
            ^2;
194
195     % Backward difference for last point
196     curvature(end) = (2*MS(end) - 5*MS(end-1) + 4*MS(end-2) -
            MS(end-3)) / dx^2;
197 end
198
```

```
199 function smoothed = GSM(data, gap)
200     % Gapped Smoothing Method: average neighboring values
        excluding the current point.
201     n = length(data);
202     smoothed = zeros(size(data));
203
204     for i = 1:n
205         lower = max(1, i - gap);
206         upper = min(n, i + gap);
207         indices = setdiff(lower:upper, i);
208         smoothed(i) = mean(data(indices));
209     end
210 end
211
212 function DI = compute_cornwell_index(phi_intact, phi_damaged,
    h)
213     % Compute the Cornwell index for each element of the beam
        .
214     nNodes = length(phi_intact);
215     kappa_intact = zeros(1, nNodes);
216     kappa_damaged = zeros(1, nNodes);
217
218     % Central difference for interior nodes
219     for j = 2:nNodes-1
220         kappa_intact(j) = (phi_intact(j-1) - 2*phi_intact(j)
            + phi_intact(j+1)) / h^2;
221         kappa_damaged(j) = (phi_damaged(j-1) - 2*phi_damaged(
            j) + phi_damaged(j+1)) / h^2;
222     end
223
224     % Forward/backward difference for boundary nodes
225     kappa_intact(1)   = (phi_intact(1) - 2*phi_intact(2) +
        phi_intact(3)) / h^2;
226     kappa_intact(end) = (phi_intact(end-2) - 2*phi_intact(end
        -1) + phi_intact(end)) / h^2;
227     kappa_damaged(1)  = (phi_damaged(1) - 2*phi_damaged(2) +
        phi_damaged(3)) / h^2;
228     kappa_damaged(end)= (phi_damaged(end-2) - 2*phi_damaged(
        end-1) + phi_damaged(end)) / h^2;
229
```

```
230     % Compute strain energy density for each element (
            trapezoidal rule)
231     r_intact = zeros(1, nNodes-1);
232     r_damaged = zeros(1, nNodes-1);
233     for j = 1:nNodes-1
234         r_intact(j) = (h/2) * (kappa_intact(j)^2 +
                kappa_intact(j+1)^2);
235         r_damaged(j) = (h/2) * (kappa_damaged(j)^2 +
                kappa_damaged(j+1)^2);
236     end
237
238     % Total strain energy for normalization
239     r_total_intact = sum(r_intact);
240     r_total_damaged = sum(r_damaged);
241
242     DI = (r_intact / r_total_intact) ./ (r_damaged /
            r_total_damaged);
243     DI(1) = 0; DI(end) = 0;
244 end
245
246 function DI = compute_stubbs_index(phi_intact, phi_damaged, h
        )
247     % Compute the Stubbs index for each beam element.
248     nNodes = length(phi_intact);
249     kappa_intact = zeros(1, nNodes);
250     kappa_damaged = zeros(1, nNodes);
251
252     % Central difference for interior nodes
253     for j = 2:nNodes-1
254         kappa_intact(j) = (phi_intact(j-1) - 2*phi_intact(j)
                + phi_intact(j+1)) / h^2;
255         kappa_damaged(j) = (phi_damaged(j-1) - 2*phi_damaged(
                j) + phi_damaged(j+1)) / h^2;
256     end
257
258     % Forward/backward difference for boundary nodes
259     kappa_intact(1)   = (phi_intact(1) - 2*phi_intact(2) +
            phi_intact(3)) / h^2;
260     kappa_intact(end) = (phi_intact(end-2) - 2*phi_intact(end
            -1) + phi_intact(end)) / h^2;
```

```
261     kappa_damaged(1)   = (phi_damaged(1) - 2*phi_damaged(2) +
            phi_damaged(3)) / h^2;
262     kappa_damaged(end)= (phi_damaged(end-2) - 2*phi_damaged(
            end-1) + phi_damaged(end)) / h^2;
263
264    % Strain energy density (squared curvatures)
265     r_intact = (h/2) * (kappa_intact(1:end-1).^2 +
            kappa_intact(2:end).^2);
266     r_damaged = (h/2) * (kappa_damaged(1:end-1).^2 +
            kappa_damaged(2:end).^2);
267
268     r_total_intact = sum(r_intact);
269     r_total_damaged = sum(r_damaged);
270
271 %      DI = ((r_intact + R_intact) ./ (r_damaged + R_damaged))
        * (R_damaged / R_intact);
272     DI = (1+(r_intact / r_total_intact)) ./ (1 + (r_damaged /
            r_total_damaged));
273 end
274
275 function DI = compute_choi_index(phi_intact, phi_damaged, h)
276     % Compute the Choi index for each beam element.
277     nNodes = length(phi_intact);
278     kappa_intact = zeros(1, nNodes);
279     kappa_damaged = zeros(1, nNodes);
280
281     % Central difference for interior nodes
282     for j = 2:nNodes-1
283         kappa_intact(j) = (phi_intact(j-1) - 2*phi_intact(j)
                + phi_intact(j+1)) / h^2;
284         kappa_damaged(j) = (phi_damaged(j-1) - 2*phi_damaged(
                j) + phi_damaged(j+1)) / h^2;
285     end
286
287     % Forward/backward difference for boundary nodes
288     kappa_intact(1)    = (phi_intact(1) - 2*phi_intact(2) +
            phi_intact(3)) / h^2;
289     kappa_intact(end) = (phi_intact(end-2) - 2*phi_intact(end
            -1) + phi_intact(end)) / h^2;
```

```
290     kappa_damaged(1)   = (phi_damaged(1) - 2*phi_damaged(2) +
            phi_damaged(3)) / h^2;
291     kappa_damaged(end)= (phi_damaged(end-2) - 2*phi_damaged(
            end-1) + phi_damaged(end)) / h^2;
292
293     % Use squared curvature instead of absolute values
294     integral_intact = (h/2) * (kappa_intact(1:end-1).^2 +
            kappa_intact(2:end).^2);
295     integral_damaged = (h/2) * (kappa_damaged(1:end-1).^2 +
            kappa_damaged(2:end).^2);
296
297     DI = (1 + integral_intact) ./ (1 + integral_damaged);
298 end
299
300 function [macro_idx, damage_flags] = compute_macro_index(
        Cornwell, Stubbs, Choi, theta)
301     % Compute macro-index and damage flags
302     % Inputs:
303     %   Cornwall, Stubbs, Choi: Damage indices (1x(nNodes-1))
304     %   theta: Detection threshold (optional)
305     % Outputs:
306     %   macro_idx: Combined damage index (1x(nNodes-1))
307     %   damage_flags: Binary damage indicators (1x(nNodes-1))
308
309  % Normalize indices per element (not global Z-score)
310     norm_Cornwell = (Cornwell - mean(Cornwell)) / std(
            Cornwell);
311     norm_Stubbs = (Stubbs - mean(Stubbs)) / std(Stubbs);
312     norm_Choi = (Choi - mean(Choi)) / std(Choi);
313
314     % Two-stage approach
315     agreement_mask = (norm_Cornwell > 0) & (norm_Stubbs > 0)
            & (norm_Choi > 0);
316     macro_idx = mean([norm_Cornwell; norm_Stubbs; norm_Choi],
             1);
317     macro_idx(~agreement_mask) = 0; % Disregard non-agreeing
            elements
318
319     % Apply threshold if provided
320     if nargin > 3
```

```
321         damage_flags = macro_idx >= theta;
322     else
323         damage_flags = [];
324     end
325 end
326
327 function [macro_idx, damage_flags] =
    compute_macro_index_weighed(norm_Cornwell, norm_Stubbs,
    norm_Choi, theta)
328     % Compute macro-index with weighted emphasis on Cornwell
329     % Weights: Cornwell (70%), Stubbs (15%), Choi (15%)
330
331     % Normalize indices using Z-score
332
333     % Apply weights: Cornwell dominates
334     weights = [0.1, 0.45, 0.45]; % [Cornwell, Stubbs, Choi]
335     weighted_indices = weights(1)*norm_Cornwell + ...
336                        weights(2)*norm_Stubbs + ...
337                        weights(3)*norm_Choi;
338
339     % Two-stage approach
340     agreement_mask = (norm_Cornwell > 0) & (norm_Stubbs > 0)
        & (norm_Choi > 0);
341     macro_idx = weighted_indices;
342     macro_idx(~agreement_mask) = 0; % Disregard non-agreeing
        elements
343
344     % Apply threshold if provided
345     if nargin > 3
346         damage_flags = macro_idx >= theta;
347     else
348         damage_flags = [];
349     end
350 end
351
352 function theta_opt = determine_threshold(phi_intact, h,
    varargin)
353     % Determine optimal damage detection threshold using
        Monte Carlo simulations
354     % Inputs:
```

```
355     %   phi_intact: Mode shape matrix of intact beam [nModes
            x nNodes]
356     %   h: Sensor spacing
357     %   varargin: {N_mc (trials), confidence_level}
358     % Output:
359     %   theta_opt: Optimal threshold for macro-index
360
361     % Parse inputs
362     p = inputParser;
363     addOptional(p, 'N_mc', 1000, @isnumeric);
364     addOptional(p, 'confidence', 0.95, @isnumeric);
365     parse(p, varargin{:});
366
367     N_mc = p.Results.N_mc;
368     conf = p.Results.confidence;
369
370     % 1. Estimate noise from intact data
371     noise_std = std(phi_intact, 0, 1); % Std. dev across
            modes
372
373     % 2. Monte Carlo simulation
374     macro_indices = [];
375     for k = 1:N_mc
376         % Generate synthetic intact/damaged data
377         phi_synth = phi_intact + noise_std .* randn(size(
                phi_intact));
378         phi_damaged = phi_synth;
379
380         % Simulate random damage (5-15% stiffness reduction
                in 1-2 elements)
381         damage_elements = randperm(size(phi_intact,2)-1,
                randi(2));
382         phi_damaged(:,damage_elements) = phi_damaged(:,
                damage_elements) .* (0.85 + 0.1*rand());
383
384         % Compute all indices
385         [Cornwell, Stubbs, Choi] = compute_all_indices(
                phi_intact, phi_damaged, h);
386
387         % Compute macro-index
```

```
388         macro_idx = compute_macro_index(Cornwell, Stubbs,
                Choi);
389         macro_indices = [macro_indices; macro_idx];
390     end
391
392     % 3. Determine threshold via percentile
393     theta_opt = prctile(macro_indices(:), 100*(1-conf));
394 end
395
396 function [Cornwell, Stubbs, Choi] = compute_all_indices(
        phi_intact, phi_damaged, h)
397     % Wrapper for index calculations
398     Cornwell = compute_cornwell_index(phi_intact, phi_damaged
            , h);
399     Stubbs = compute_stubbs_index(phi_intact, phi_damaged, h)
            ;
400     Choi = compute_choi_index(phi_intact, phi_damaged, h);
401 end
```

APPENDIX C: SAMPLE MAPDL CODE

```
/PREP7

! Element type (3D 20-node solid)
ET,1,SOLID186

! Material Properties
MP,EX,1,3000.8e6        ! Young's modulus of fiberglass
   composite beam in Pa
MP,PRXY,1,0.33          ! Poisson's ratio
MP,DENS,1,1200          ! Density in kg/m^3

! --- Geometry Creation ---

! Geometric properties
L = 0.120       ! Length of beam in m
W = 0.025       ! Width of beam in m
T = 0.002       ! Thickness of beam in m

BLOCK, 0, L, 0, T, 0, W

! meshing
ESIZE, 0.5/1000         ! Element size in m
VMESH, ALL              ! Meshing the entire volume

! Boundary Condition (Cantilever Constraint) ---
! Fixing the face at X=0 (all DOFs) for a cantilever beam
NSEL, S, LOC, X, 0
D, ALL, ALL
ALLSEL

FINISH

/SOLU
! --- Modal Analysis Setup ---
ANTYPE, MODAL
MODOPT, LANB, 10        ! Block Lanczos algorithm for 10 modes
MXPAND, 10              ! Expanding 10 mode shapes for
   postprocessing
```

```
37 SOLVE
38 FINISH
39
40 /POST1
41 ! --- Postprocessing ---
42 SET,1,1                ! Selecting the first mode result for
      display
43 PLDISP,2               ! Plotting the deformed mode shape (
      scale factor 2)
44 FINISH
```

Listing 1: ANSYS APDL Code for Modal Analysis

LETTER OF PAPER SUBMISSION AT JIE

Pulchowk Campus
Institute of Engineering
Tribhuvan University

AAYUSH BHATTA <079msmde001.aayush@pcampus.edu.np>

[jie] Submission Acknowledgement

Prof. Dr. Hem Raj Pant <tuta@pcampus.edu.np> Tue, Apr 1, 2025 at 6:34 AM
To: Aayush Bhatta <079msmde001.aayush@pcampus.edu.np>

Aayush Bhatta:

Thank you for submitting the manuscript, "Damage Detection in Composite Beams Using Modal Curvature Based Techniques" to Journal of the Institute of Engineering. With the online journal management system that we are using, you will be able to track its progress through the editorial process by logging in to the journal web site:

Submission URL: https://tuta.pcampus.edu.np/journal/index.php/jie/authorDashboard/submission/156
[Quoted text hidden]

SIMILARITY REPORT

Aayush Bhatta

Delamination detection in composite beams using modal curvature based techniques

Tribhuvan University

Document Details

Submission ID
trn:oid:::3117:450275057

Submission Date
Apr 18, 2025, 5:37 PM GMT+5:45

Download Date
Apr 18, 2025, 5:38 PM GMT+5:45

File Name
079MSMDE001_Final_Thesis (1).pdf

File Size
3.3 MB

34 Pages

9,035 Words

47,788 Characters

iThenticate Page 1 of 38 - Cover Page Submission ID trn:oid:::3117:450275057

3% Overall Similarity

The combined total of all matches, including overlapping sources, for each database.

Filtered from the Report

- Bibliography
- Quoted Text
- Cited Text
- Small Matches (less than 8 words)

Match Groups

- **24** Not Cited or Quoted **3%**
  Matches with neither in-text citation nor quotation marks
- **0** Missing Quotations **0%**
  Matches that are still very similar to source material
- **0** Missing Citation **0%**
  Matches that have quotation marks, but no in-text citation
- **0** Cited and Quoted **0%**
  Matches with in-text citation present, but no quotation marks

Top Sources

1% Internet sources
2% Publications
0% Submitted works (Student Papers)

Integrity Flags

1 Integrity Flag for Review

Replaced Characters
33 suspect characters on 9 pages
Letters are swapped with similar characters from another alphabet.

Our system's algorithms look deeply at a document for any inconsistencies that would set it apart from a normal submission. If we notice something strange, we flag it for you to review.

A Flag is not necessarily an indicator of a problem. However, we'd recommend you focus your attention there for further review.

Match Groups

- **24** Not Cited or Quoted 3%
  Matches with neither in-text citation nor quotation marks
- **0** Missing Quotations 0%
  Matches that are still very similar to source material
- **0** Missing Citation 0%
  Matches that have quotation marks, but no in-text citation
- **0** Cited and Quoted 0%
  Matches with in-text citation present, but no quotation marks

Top Sources

1% Internet sources
2% Publications
0% Submitted works (Student Papers)

Top Sources

The sources with the highest number of matches within the submission. Overlapping sources will not be displayed.

1	Publication	
Pankaj Chaupal, Prakash Rajendran. "A review on recent developments in vibrati...		<1%
2	Publication	
Daniele Dessi, Fabio Passacantilli, Andrea Venturi. "Analysis and mitigation of unc...		<1%
3	Publication	
Suhas Ankalkhope, Sandeep Jose. "Non-destructive characterization of cylindrical...		<1%
4	Internet	
pure.rug.nl		<1%
5	Internet	
rosap.ntl.bts.gov		<1%
6	Internet	
etd.hu.edu.et		<1%
7	Internet	
www.metrolinx.com		<1%
8	Internet	
www.coursehero.com		<1%
9	Publication	
Loan Dolbachian, Walid Harizi, Zoheir Aboura. "Experimental Linear and Nonlinea...		<1%
10	Internet	
open.library.ubc.ca		<1%